1 # Freely-moving mice visually pursue prey using a retinal

2 # area with least optic flow

3

4 Carl D. Holmgren[1], Paul Stahr[1], Damian J. Wallace, Kay-Michael Voit, Emily J. Matheson, Juergen Sawinski,

5 Giacomo Bassetto & Jason N. D. Kerr

6

7 Department of Behavior and Brain Organization, Research center caesar, 53175, Bonn, Germany

8 [1] denotes equal contribution.

9

10

11 Correspondence to:

12 Jason Kerr

13 email: jason.kerr@caesar.de

14

15 **Abstract:**

16 Mice have a large visual field that is constantly stabilized by vestibular ocular reflex driven eye rotations

17 that counter head-rotations. While maintaining their extensive visual coverage is advantageous for

18 predator detection, mice also track and capture prey using vision. However, in the freely moving animal

19 quantifying object location in the field of view is challenging. Here, we developed a method to digitally

20 reconstruct and quantify the visual scene of freely moving mice performing a visually based prey capture

21 task. By isolating the visual sense and combining a mouse eye optic model with the head and eye rotations,

22 the detailed reconstruction of the digital environment and retinal features were projected onto the

23 corneal surface for comparison, and updated throughout the behavior. By quantifying the spatial location

24 of objects in the visual scene and their motion throughout the behavior, we show that the image of the

25 prey is maintained within a small area, the functional focus, in the upper-temporal part of the retina. This

26 functional focus coincides with a region of minimal optic flow in the visual field and consequently minimal

27 motion-induced image blur during pursuit, as well as the reported high density-region of Alpha-ON

28 sustained retinal ganglion cells.

29

30 **Introduction:**

31 The visual system of mice serves a variety of seemingly opposing functions that range from detection of

32 predators, to finding shelter and selection of food and mates, and is required to do so in a diverse set of

33 environments (Boursot, Auffray et al. 1993). For example, foraging in open areas where food is available

34 involves object selection, and in the case of insect predation (Badan 1986, Tann, Singleton et al. 1991),

35 involves prey tracking and capture (Langley 1983, Langley 1984, Langley 1988, Hoy, Yavorska et al. 2016),

36 but the visual system can also simultaneously be relied on for avoidance of predation, particularly from

37 airborne predators (Hughes 1977). Like with many ground-dwelling rodents (Johnson and Gadow 1901)

38 predator detection in mice is served by a panoramic visual field which is achieved by the lateral placement

39 of the eyes in the head (Drager 1978, Hughes 1979, Oommen and Stahl 2008) combined with monocular

40 visual fields of around 200 degrees (Hughes 1979, Drager and Olsen 1980, Sterratt, Lyngholm et al. 2013).

41 In mice, the panoramic visual field extends to cover regions above the animal's head, below the animals

42 snout and laterally to cover ipsilaterally from behind the animals head to the contralateral side, with the

43 overlapping visual fields from both eyes forming a large binocular region overhead and in front of the

44 animal (Hughes 1977, Sabbah, Gemmer et al. 2017). In addition, eye movements in freely moving mice

45 constantly stabilize the animal's visual field by counteracting head rotations through the vestibulo-ocular

46 reflex (VOR) (Payne and Raymond 2017, Meyer, Poort et al. 2018, Meyer, O'Keefe et al. 2020, Michaiel,

47 Abe et al. 2020) maintaining the large panoramic overhead view (Wallace, Greenberg et al. 2013) critical

48 for predator detection (Yilmaz and Meister 2013).

49 Given the VOR stabilized panoramic field of view it is not clear what part of the visual field mice use to

50 detect and track prey (but see: (Johnson, Fitzpatrick et al. 2021). Mouse retina contains retinal ganglion

51 cells (RGCs), the output cells of the retina, with a broad diversity of functional classes (Zhang, Kim et al.

52 2012, Bleckert, Schwartz et al. 2014, Baden, Berens et al. 2016, Franke, Berens et al. 2017). Given the

53 lateral eye position, the highest overall density faces laterally (Drager and Olsen 1981, Salinas-Navarro,

54   Jimenez-Lopez et al. 2009, Sabbah, Gemmer et al. 2017, Stabio, Sondereker et al. 2018). Further, as the

55   functionally defined ganglion cells (Zhang, Kim et al. 2012, Bleckert, Schwartz et al. 2014, Baden, Berens

56   et al. 2016, Franke, Berens et al. 2017) and cone sub-types (Szel, Rohlich et al. 1992) are segregated into

57   retinal subregions within the large stabilized field of view, recent studies suggest that retinal subregions

58   are tuned for specific behavioral tasks depending on what part of the world they subtend (Hughes 1977,

59   Zhang, Kim et al. 2012, Bleckert, Schwartz et al. 2014, Baden, Berens et al. 2016, Sabbah, Gemmer et al.

60   2017, Szatko, Korympidou et al. 2020).

61   The challenge is to measure what part of the visual field the mouse is attending to during a visually based

62   tracking task (Hoy, Yavorska et al. 2016) and the location of all objects within the field of view during the

63   behavior. While recent studies have implied the relationship between prey and retina through tracking

64   head position (Johnson, Fitzpatrick et al. 2021) or measured both the horizontal and vertical eye rotations

65   (Meyer, Poort et al. 2018, Meyer, O'Keefe et al. 2020) during pursuit behavior (Michaiel, Abe et al. 2020)

66   to uncover a large proportion of stabilizing eye-rotations, what is missing is the extent and location of the

67   area used when detecting and pursuing prey, and the relationship to the retina (Bleckert, Schwartz et al.

68   2014).

69   Here, we measured the position of a cricket in the visual fields of freely moving mice performing a prey

70   pursuit behavior, using head and eye tracking in all three rotational axes, namely horizontal, vertical and

71   torsional. Eye tracking included an anatomical calibration to accurately account for the anatomical

72   positions of both eyes. To quantify object location in the animal's field of view and generate optic flow

73   fields, head and eye rotations were combined with a high-resolution digital reconstruction of the arena

74   to form a detailed visual map from the animal's eye perspective. Given that mice use multisensory

75   strategies during prey pursuit (Langley 1983, Langley 1988, Gire, Kapoor et al. 2016) and can track prey

76   using auditory, visual or olfactory cues (Langley 1983, Langley 1988), we developed a behavioral arena

77   that isolated the visual aspect of the behavior by removing auditory and olfactory directional cues to

78   ensure that the behavior was visually guided. To transfer the retinal topography onto the corneal surface,

79   we developed an eye model capturing the optical properties of the mouse eye. We show that during prey

80   detection mice preferentially position prey objects in stable foci located in the binocular field and

81   undertake direct pursuit. The stabilized functional foci are spatially distinct from the regions of highest

82   total retinal ganglion cell density, which are directed laterally, but coincides with the regions of the visual

83   field where there is minimal optic flow and therefore minimal motion-induced image disturbance during

84   the behavior. Lastly, by building an optical model that allows corneal spatial locations to be projected onto

85   the retina, we suggest that the functional foci correspond to retinal subregions containing a large density

86   of Alpha-ON sustained RGCs that have center-surround receptive fields and project to both superior

87   colliculus and dLGN (Huberman, Manu et al. 2008) and possess properties consistent with the

88   requirements for tracking small and mobile targets (Krieger, Qiao et al. 2017).

89

90   **Results:**

91   **Forming a view from the animal's point of view**

92   To measure what part of the visual field mice use during prey capture while also considering that mice

93   can use multisensory strategies during prey pursuit (Langley 1983, Langley 1988, Gire, Kapoor et al. 2016),

94   we first developed an arena which isolated the visual component of prey pursuit by masking olfactory and

95   auditory spatial cues (Figure 1A, see Methods for details). By removing both olfactory and auditory cues,

96   the average time to capture a cricket approximately doubled compared to removal of auditory cues alone

97   (time to capture, median±SD, control 24.92±16.77s, olfactory & auditory cues removed, 43.51±27.82s,

98   p=0.0471, Wilcoxon rank sum test, N=13 control and 12 cue removed trials from N = 5 mice). To track

99   mouse head and eye rotations during prey capture, we further developed a lightweight version of our

100   head mounted oculo-videography and camera-based pose and position tracking system (Wallace,

101   Greenberg et al. 2013) (Figure 1B and Methods, Figure 7 A and B). This approach allowed quantification

102   of head rotations in all three axes of rotation (pitch, roll and yaw), as well as eye rotations in all three

103   ocular rotation axes (torsion, horizontal and vertical, Figure 1C, Figure 1 – figure supplement 1 A and B).

104   The same videography-based system was used to track and triangulate the position of the cricket (see

105   Methods and Figure 1 – figure supplement 1C). To quantify the position and motion of the environment

106   and cricket in the mouse field of view, we also developed a method that enabled a calibrated environment

107   digitization to be projected onto the corneal surface. This approach utilized a combination of laser

108   scanning and photogrammetry, giving a resolution for the reconstruction of the entire experimental room

109   of 2 mm, as well as a detailed measurement of eye and head rotations (Figure 1D-E, and see methods).

110   Mice, like rats (Wallace, Greenberg et al. 2013), have a large visual field of view which extends to also

111   cover the region over the animal's head (Figure 1F). To ensure the entire visual fields of the mouse could

112   be captured during behavior, we digitized the entire experimental room and contents (Figure 1E, Figure 1

113   – figure supplement 1D-F, Movie 1). The coordinate systems of the environmental digitization and mouse
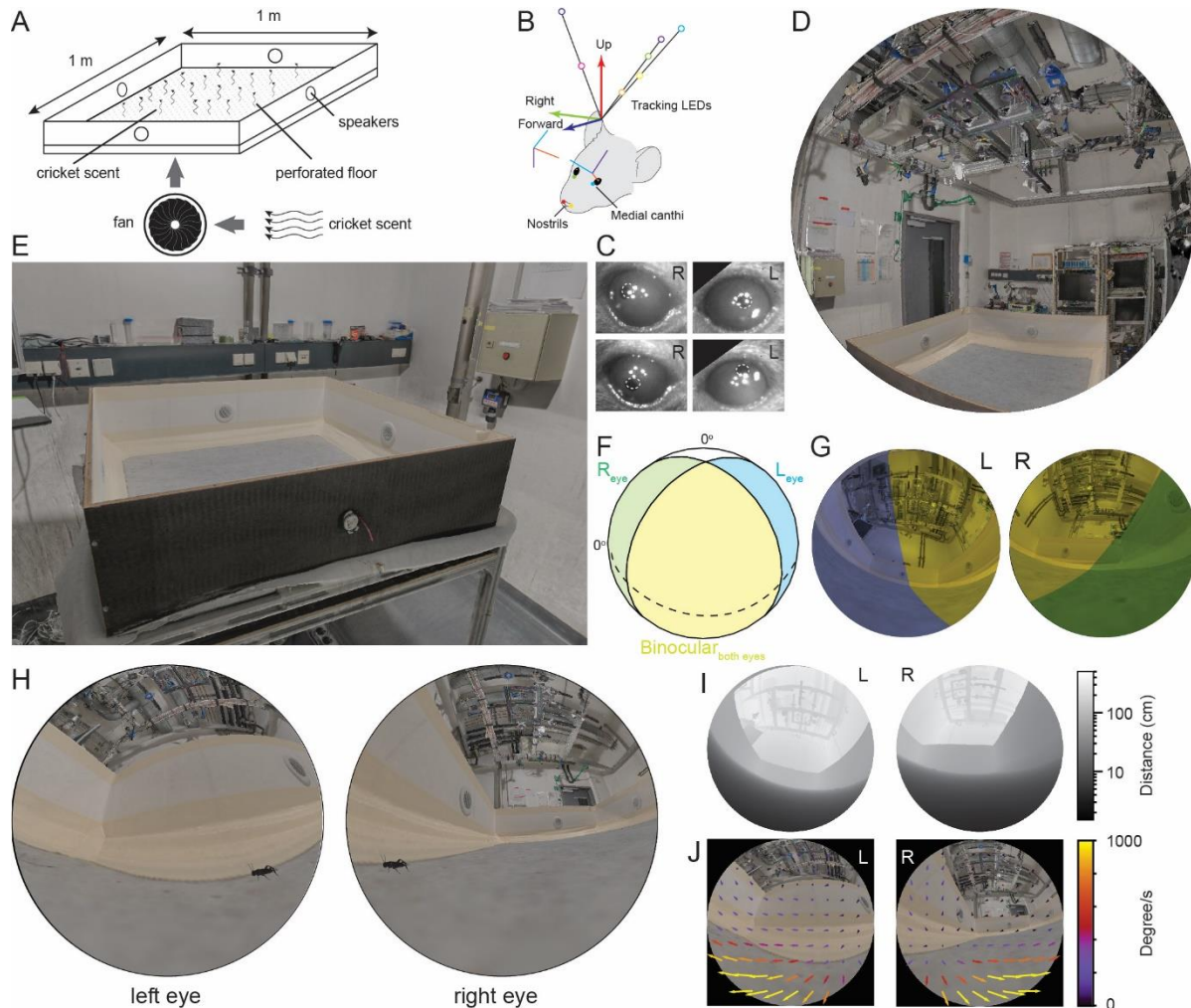
6

114

Figure 1 with 1 supplement
Reconstruction of experimental arena and surrounds from the animal's perspective.
(A) Schematic of experimental arena with olfactory and auditory noise. (B) Schematic of tracking, ana-tomical and eye camera calibration. Head position and orientation was tracked using seven IR-LEDs (colored circles). Nostrils (red, yellow filled circles), left (blue filled circle) and right (green filled circle) medial canthi were identified and triangulated in calibration images and used to define a common coor-dinate system (forward, blue arrow, right, green arrow, and up, red arrow), into which the calibrated eye camera location and orientation could also be placed (eye camera vertical, cyan, horizontal, purple, camera optical axis, red). (C) Example left- and right eye camera images with tracked pupil position (white dashed outlines). (D) Rendered digital reconstruction of the laboratory room and (E) experimental arena. (F) Schematic representation of mouse's left- (blue) and right (green) visual fields, showing also the region of binocular overlap (yellow) and un-seen region (white). (G) Reconstruction of the arena and room from the animal's left- and right eye perspective, with monocular and binocular regions colored as in (F). (H) Reconstruction of the animal's view of the prey (cricket - black) in the experiment arena. (I) Representation of left and right eye views of the arena and surrounding objects grayscale-coded by distance from the eye. (J) Rendered animal's eye views from the left- and right eyes with overlay of arrows representing optic flow during 10 ms during free motion.

115

116   and cricket tracking systems were registered using 16-20 fiducial markers identified in both the overhead

117   camera images and the digitized environment. The average differences in position of fiducial points

118   between the two coordinate systems were less than 1 mm (mean±SD, x position, 0.18±3.1mm, y position,

119   0.07±1.6mm, z position, 0.66±1.8mm, N=54 fiducial points from 3 datasets). The next step was to re-

120   create the view for each eye. First, and for each mouse, the positions of both eyes and nostrils were

121   measured with respect to both the head-rotation tracking LEDs and head-mounted cameras, then

122   calibrated into a common coordinate system (Figure 1B). Together, this enabled a rendered

123   representation of the digitized field of view for each combination of head and eye rotations. This rendered

124   image, from the animal's point of view, contained all the arena and lab objects (Figure 1G-H, Movie 2,

125   Figure 1 – figure supplement 1G). In addition, to object position and distance (Figure 1I), the motion of

126   the environment and each object in the field of view could be quantified as the mouse performed prey

127   capture behaviors (Figure 1J, and Figure 1 – figure supplement 1H).

128

129   **Mice keep prey in a localized visual region during pursuit**

130   Crickets (*Acheta domesticus*), shown previously to be readily pursued and preyed upon by laboratory mice

131   (Hoy, Yavorska et al. 2016), provided a prey target that could successfully evade capture for extended

132   periods of time (total time for each cricket before capture: 64.4±39.3 s, average time±SD, N=21 crickets

133   and 3 mice). To ensure that only data where the mouse was actively engaged in the detection and tracking

134   of the cricket was used, we identified occasions where the mouse either captured the cricket, or contacted

135   the cricket but the cricket escaped (see Methods for definitions), and then quantified the trajectories of

136   both mouse and cricket leading up to the capture or capture-escape (Figure 2A). Within these chase

137   sequences we defined three behavioral epochs (detect, track and capture, Figure 2B, see Methods for
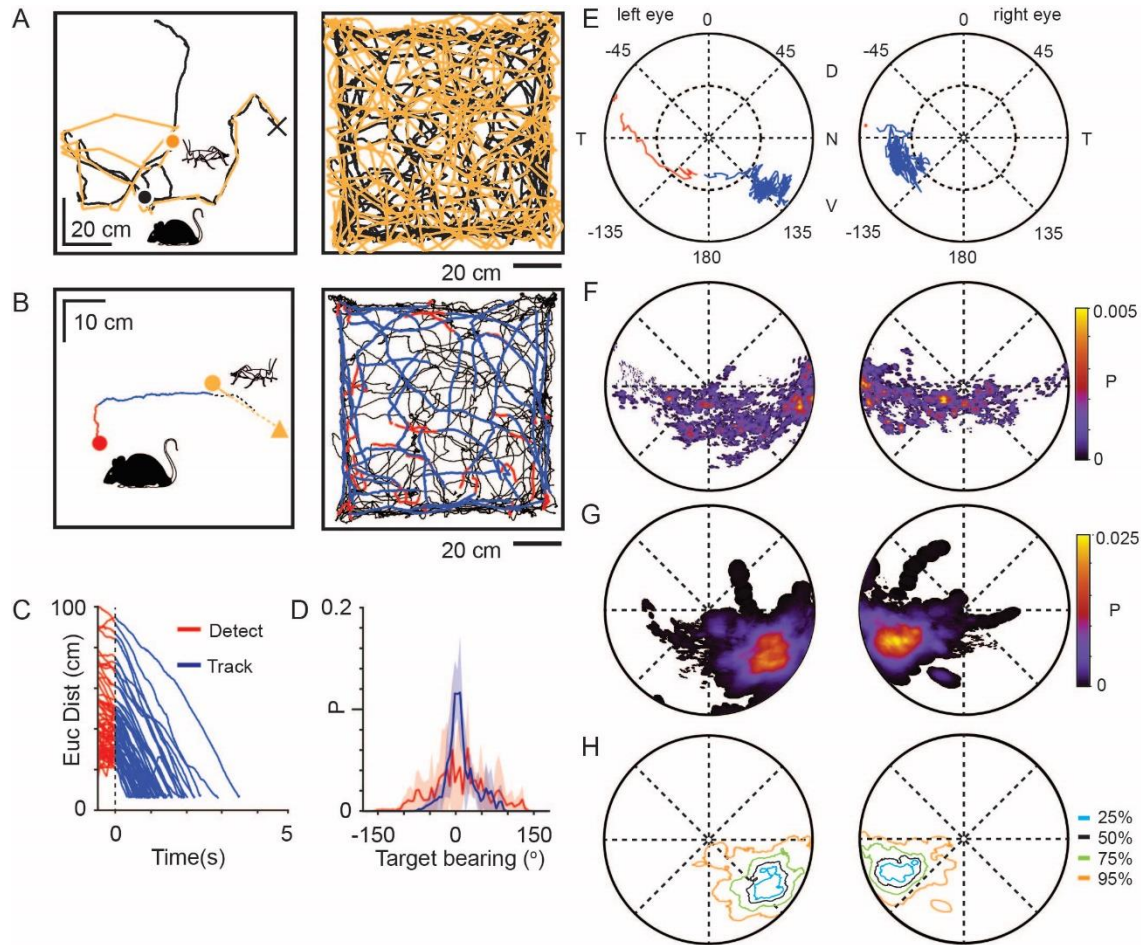
138

Figure 2 with 1 supplement
Mice use a focal region of their visual field to track prey.
(A) Mouse (black) and cricket (orange) paths during a single pursuit sequence (left), and for all pursuit sequences in one session for one animal (right). Pursuit start denoted as filled circles and cricket capture as X. **(B)** Mouse (red and blue) and cricket (orange) paths during an individual pursuit sequence (left) and all pursuit sequences in one session from one animal (right), showing detect (red) and track (blue) epochs of the mouse path. Paths after a cricket escape shown dashed. Pursuit sequence start shown as filled circles, cricket landing point after a jump shown as a filled triangle. **(C)** Euclidean distance between mouse and cricket during detect (red) and track (blue) epochs (n=65 trajectories, n=3 mice). **(D)** Mean and SD bearing to cricket (angle between mouse's forward direction and cricket location) during detect (red), and track (blue) epochs for all sequences from all animals (detect: 57 epochs, 4406 frames; track: 65 epochs, 13624 frames, n=3 animals, bin size = 5o). **(E)** Trajectory of the projected cricket position in the left and right corneal views, during a single pursuit sequence. Color scheme as for D. The inner dashed circle is 45o from the optical axes. Dorsal (D), ventral (V), nasal (N) and temporal (T) directions indicated. **(F)** Average probability density maps for detect epochs (4628 frames from 3 animals). Orientation as in E. **(G)** Average probability density maps for track epochs (13641 frames from 3 animals). Orientation as in E. **(H)** Isodensity contours calculated from the average probability density maps for track epochs. (note that 50% means that this region contains 50% of the total density, and likewise for the other contours). Orientation as in E.

140   definition details) based on the behavior of mouse and cricket, and similar to previous studies (Hoy,

141   Yavorska et al. 2016).

142   Upon cricket detection, mice oriented and ran towards the cricket, resulting in a significant adjustment to

143   their trajectory (Δ target bearing: 40.2±35.1°, P=6.20X10^{-10}, Δ speed: 10.2±7.4cm/s, P=1.91X10^{-10}; N=57

144   detect-track sequences N = 3 mice; Paired Wilcoxon's signed rank test for both tests), and a rapid

145   reduction in the Euclidean distance to the cricket (Figure 2C). During tracking, the cricket was kept in front

146   of the mouse, resulting in a significant reduction in the spread of target bearings compared to during

147   detect epochs (Figure 2D, Target bearing: detect 6.2± 62.1°, track: 2.5 ±25.6°, mean±SD, Brown-Forsythe

148   test p=0, *F* statistic=7.05x10^3, N=4406 detect and 13624 track frames, N=3 mice), consistent with previous

149   findings (Hoy, Yavorska et al. 2016). To avoid the closing phase of the pursuit being associated with

150   whisker strikes (Shang, Liu et al. 2019, Zhao, Chen et al. 2019), tracking periods were only analyzed when

151   the mouse was more than 3 cm from the cricket, based on whisker length (Ibrahim and Wright 1975).

152   Using the detailed digitization of the behavioral arena and surrounding laboratory method (Figure 1E,

153   Movie 1), an image of the cricket and objects in the environment was calculated for each head and eye

154   position during the predator-prey interaction (Movie 2). Using this approach, we addressed the question

155   of what area of the visual field was the cricket located in during the various behavioral epochs. In the

156   example pursuit sequence in Figure 2E the cricket was initially located in the peripheral visual field and

157   then transitioned to the lower nasal binocular quadrant of the cornea-view during pursuit and capture

158   (red trace in left eye to blue trace in both eyes). Correspondingly, an average probability density map

159   calculated for all animals during the detect epoch showed a very broad distribution of cricket positions

160   across the visual field (Figure 2F, Figure 2 – figure supplement 1A and B). Upon detection the mouse

161   oriented towards the cricket, bringing it towards the lower nasal binocular visual field (Figure 2E). When

162   averaged for all pursuit sequences from all animals, projected cricket positions formed a dense cluster on

163   the cornea of both eyes (Figures 2G and 2H, Figure 2 – figure supplement 1A, C-D, 50% contour center for

164   left and right eye respectively, radial displacement from optical axis 64.3±7.5° and 63.3±9.9°, rotational

165   angle 126.2±8.9° and -115.7±6.1°, mean ± SD, N= 3 mice), which was significantly different from the

166   cluster in the detect epoch (average histogram of the location of cricket image during tracking phase vs

167   average histogram of the location of cricket during detect phase: Left eye P=3.54x10^{-46}, Right eye

168   P=1.08x10^{-81}, differences calculated by taking the Mean Absolute Difference with bootstrapping, N=57

169   detect-track sequences, N = 3 mice). Thus, despite mice lacking a retinal fovea (Drager and Olsen 1981,

170   Jeon, Strettoi et al. 1998), the image of the prey is kept on a local and specific retinal area during the

171   tracking and pursuit behavior. The image of the prey was localized on a specific region of retina within the

172   binocular field, while the region of elevated density of RGCs has been found to be located near the optical

173   axis (Drager and Olsen 1981), which suggests that the location of the retinal specialization may not overlap

174   with the functional focus.

175   **Functional foci do not overlap with highest ganglion cell density**

176   To determine whether the identified functional focus spatially overlaps with the area of highest density

177   of retinal ganglion cells we made a mouse eye-model (Figure 3A), modified from previous models (Barathi,

178   Boopathi et al. 2008). Using the eye model, retinal spatial locations could be projected through the optics

179   of the mouse eye to the corneal surface. We first reconstructed the isodensity contours of published RGCs

180   (Drager and Olsen 1981) to define the retinal location of the mouse retinal specialization (Figure 3- figure

181   supplement 1A-C, note that these contours are also in agreement with other recently published maps of

182   total RGC density (Zhang, Kim et al. 2012, Bleckert, Schwartz et al. 2014)). The lens optical properties were

183   based on a GRIN lens (present in both rats (Philipson 1969, Hughes 1979) and mice (Chakraborty, Lacy et

184   al. 2014)). To determine the optical characteristics of this lens we developed a method which combined

185   models of the lens surface and refractive index gradient (Figure 3A, Figure 3- figure supplement 1D and

186   Tables 1 and 2, see methods for details). Using this model, the contours representing the retinal

187   specializations were projected through the eye model onto the corneal surface to determine equivalent
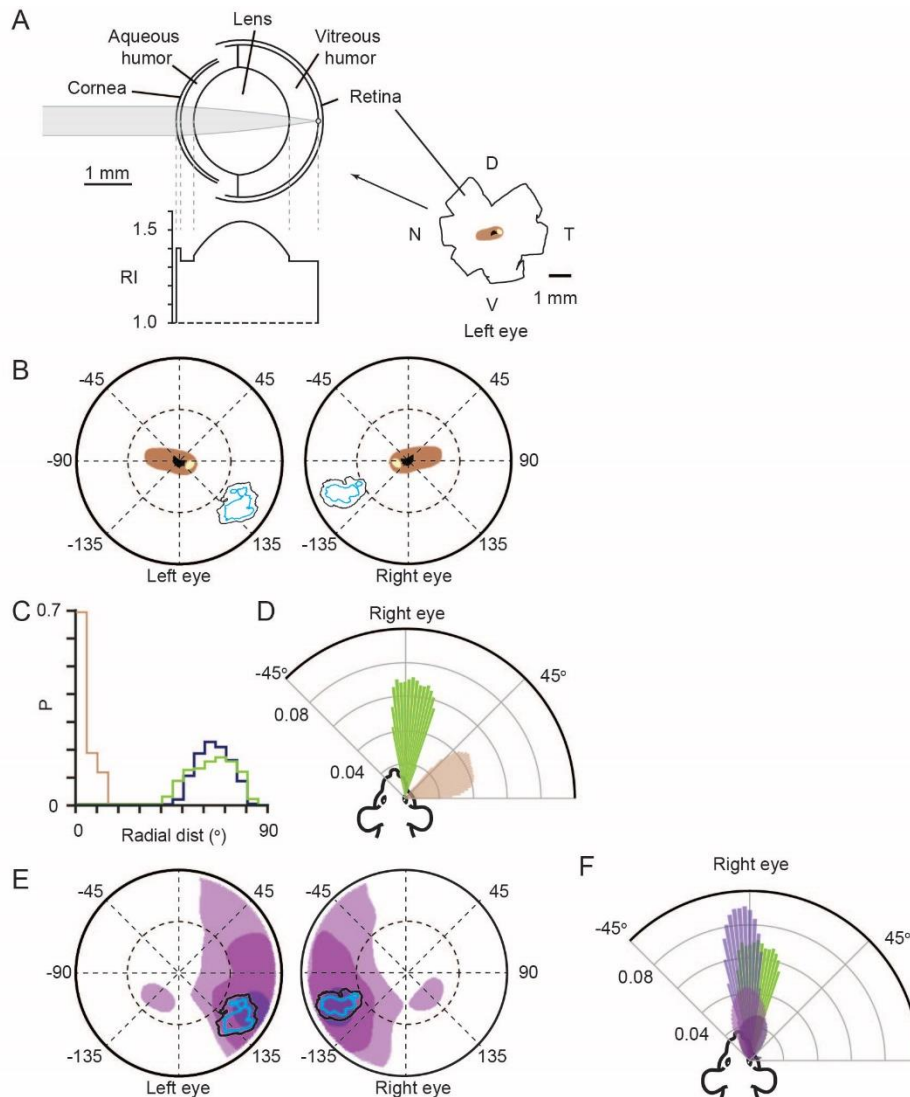
188   11

Figure 3 with 1 supplement
Functional foci are not sampled by the highest density retinal ganglion cell region.
(A) Schematic of mouse eye model (left upper) with profile of all refractive indices (RI, left lower). Reconstructions of the optic disc (black), highest (>8000 cells/mm^2, beige) and second highest (>7000 cells/mm^2, brown) retinal ganglion cell (RGC) density regions redrawn from Drager & Olsen 1981, shown in lower right. **(B)** Position in corneal views of the high RGC density regions (brown and beige filled regions), and isodensity contours from Figure 2H after projection through the eye model. Orientation as in Figure 2E. **(C)** Horizontal axis histograms for the nasal half of the corneal view of the second highest RGC region (brown) and 50% isodensity contour for left (blue) and right (green) eyes. **(D)** Top-down view of the coverage regions for the right eye of the 50% isodensity contour (green, N = 7551 frames) and second highest RGC region (brown, N = 51007 frames) for a single animal. Bars represent the probability density function for the respective regions at that azimuth angle. **(E)** Position in corneal views of Alpha-ON sustained RGC densities (redrawn from Bleckert et al. 2014) after projection through the eye model. Colored regions show the 95% (dark purple), 75% (medium purple) and 50% (light purple) contour regions of the peak Alpha-ON sustained RGC density. Isodensity contours from Figure 2H. **(F)** Top-down view of the coverage regions for the right eye of the 95% (dark purple), 75% (medium purple) and 50% (light purple) Alpha-ON sustained RGC contour regions (same as in E, N = 51007 frames) and the 50% isodensity contour from D (green) for a single animal. For the Alpha-ON sustained RGC contour regions 50% means that this region contains all points which are at least 50% of the peak RGC density.

189

190   corneal locations (Figure 3B, Figure 3- figure supplement 1E). Comparing this corneal projected location

191   to the functional focus location showed that the region with the highest RGC counts had no overlap with

192   the functional focus (Figure 3B) and occupied non-overlapping peripheral locations (Figure 3C). Viewed

193   from above the animal's head the functional foci were directed at the region in front of the animal's nose

194   and within the region of stable binocular overlap (azimuth: 1.4±8.8° and -4.4±9.3°, elevation 5.7±2.1° and

195   4.9±1.4° for left and right eyes respectively, N = 13641 frames, N=3 mice), while the retinal specialization

196   was directed laterally (azimuth: -66.2 ±6.7° and 70.3±4.7°, elevation: 30.8±12.2° and 41.0±13.5° for left

197   and right eyes respectively, N = 13641 frames N=3 mice. Figure 3D, Figure 3 – figure supplement 1F-G).

198   As the projected location of the RGC high density region and the functional focus are both sensitive to

199   torsional offsets and the location of the RGC region is also sensitive to the selected location for the optical

200   axis of the eye model, we next measured what rotational transformations would be required for the RGC

201   high density region and the functional focus to overlap. The size and locations of the two regions are such

202   that there is no torsional rotation which would produce overlap (Figure 3 – figure supplement 1H-K). Any

203   overlap of the regions would then require a large offset in the placement of the optical axis of the eye

204   model on the redrawn retinal whole mount. Here we aligned the optical axis of the eye model with the

205   center of mass of the redrawn optic disc, which has been measured as being 3.7° from the geometrical

206   center of the retina (Sterratt, Lyngholm et al. 2013). As the spherical distance between the centers of the

207   two regions was 52° (mean±SD, Left, 52.9±1.4°; Right, 51.4±4.6°, n=3 mice), no reasonable offsets or

208   errors could result in overlap. Together this shows that that although mice maintain their prey within a

209   focal visual region during the tracking phase of their pursuit behavior, this region does not overlap with

210   the visual space represented by overall highest density RGC region of the retina (Drager and Olsen 1981,

211   Jeon, Strettoi et al. 1998, Zhang, Kim et al. 2012). As a high-density of Alpha-ON sustained RGC's are

212   spatially located on the dorso-temporal retina (Bleckert, Schwartz et al. 2014), consistent with projecting

213

214   **Table 1. Mouse eye model curvatures**

215   Radii of curvature of the optical components of the mouse eye model in Figure 3A.

216

Ocular Component	Radius of curvature (μm)
Anterior Cornea	-1408*
Posterior Cornea	-1372*
Anterior Lens	-1150*
Posterior Lens	1134*
Retina	1598*

225   * -values from (Barathi, Boopathi et al. 2008)

226

227   **Table 2. Mouse eye model thicknesses and refractive indices**

228   Parameters for the mouse eye model in Figure 3A.

229

Ocular Component	Thickness(μm)	Index of refraction
Cornea	92*	1.402*
Anterior chamber	278*	1.334*
Lens	2004*	*1.36 – 1.55#*
Vitreous chamber	609*	1.333*

236   * - values from (Barathi, Boopathi et al. 2008)

237   # - minimum and maximum values after eye model optimization.

238

239 to the front of the animal, we next quantified whether this region overlapped with the functional focus

240 observed here (Figure 3E).

241 The average 50% contour of the functional focus was overlapped by the highest density of On Alpha-ON

242 sustained RGC's by 35 and 67% for left and right eye respectively (Figure 3E, black, mean±SD for left and

243 right eye, 35.1±19.8 %, 66.7±0.09 %, p= 0.095 & 0.019, one-sided Student's t-test), and for the overlap

244 with the second highest density was 83 and 95% (mean±SD for left and right eye, 82.8±20.1 %, 94.8±24.7

245 %, p= 0.042 & 0.003, one-sided Student's t-test), suggesting a high degree of correspondence between

246 the highest density of Alpha-ON sustained RGC's and the functional focus during pursuit behavior. Viewed

247 from above the animal's head the functional foci were directed at the region in front of the animal's nose

248 azimuth: 1.4±8.8° and -4.4±9.3°, elevation: 5.7±2.1° and 4.9±1.4° for left and right eyes respectively, N =

249 13641 frames, N=3 mice). The Alpha-ON sustained RGC's were also directed in front of the animal's nose

250 (mean±SD, elevation:16.0±6.9° and 10.8±11.0 °, azimuth: -3.6±0.7 ° and 5.8±7.9 ° for left and right eyes

251 respectively, N = 168400 frames, N=3 mice, Figure 3F). Together this suggests that objects falling within

252 the functional foci are processed by Alpha-ON sustained RGC's.

253 **Combination of torsional, horizontal, and vertical eye rotations counter head rotations**

254 Eye movements in freely moving mice, like with rats (Wallace, Greenberg et al. 2013), can be large and

255 rapid (Payne and Raymond 2017, Meyer, O'Keefe et al. 2020), and counter head rotations through the

256 VOR (Figure 4 – figure supplement 1), enabling the large field of view around the animals head to be

257 stabilized while the animal is moving. While the relationships between head rotations and both the

258 horizontal and vertical eye rotations have been quantified, how these rotations combine with torsional

259 rotations is not known. If mouse VOR operates similar to that observed in the rat (Wallace, Greenberg et

260 al. 2013), torsional rotations in the mouse will play a significant role in stabilizing the visual field

261 particularly during changes in head pitch. As with the vertical and horizontal rotations (Meyer, Poort et
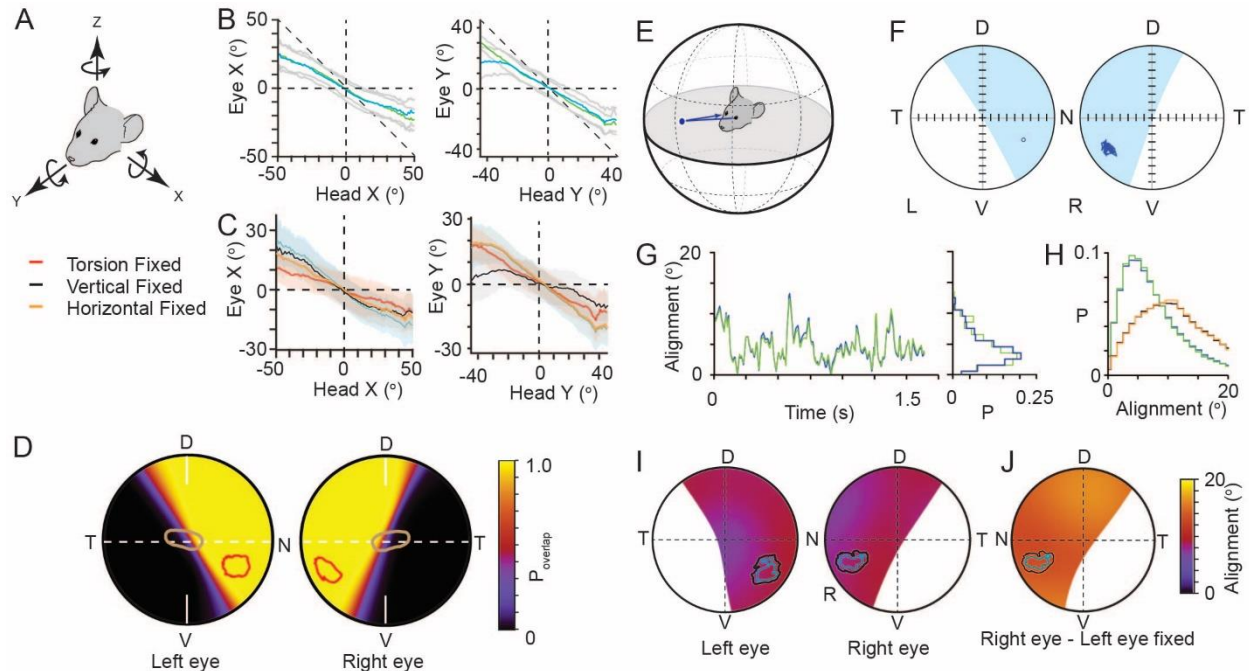
262

Figure 4 with 3 supplements
Functional foci are located within binocular regions in which motion is stabilized.
(A) Schematic of the common head and eye rotational axes. **(B)** Relationship between head and eye rotations around the common X (left, 154500 frames from 3 animals) and Y (right, 165345 frames from 3 animals) rotational axes during pursuit and non-pursuit sequences. Plots show mean for left (blue) and right (green) eyes with standard deviation (gray). **(C)** Relationship between head and left eye rotations around the common X (left) and Y (right) rotational axes with; all eye rotations present (blue), torsional eye rotations frozen (red), vertical eye rotations frozen (black) or horizontal eye rotations frozen (orange). Plots show mean (lines) and standard deviations (colored filled regions). **(D)** Corneal view showing probability of overlap of left and right visual fields for one example animal (71995 frames), with overlay of isodensity contours (red) from functional foci (see Figure 2 – figure supplement 1D) and contour of second highest RGC region (brown) from Figure 3B. **(E)** Schematic of inter-ocular alignment. **(F)** Corneal view of alignment reference point in left eye (left) and variability in alignment of the re-projection of that point in the right eye (right) for a 1.6s data segment. **(G)** Kinetics (left) and associated distribution (right) of the variability in ocular alignment for left eye point projected to right eye (blue) and right eye point in left eye (green) for one example data segment (shown in G) from one animal. **(H)** Distributions of ocular alignment from all data segments (159318 frames, n=3 mice) with the measured eye movements for left into right eye (blue) and right into left eye (green) and alignment with eye movements frozen (left into right eye, black, right into left, orange). **(I)** Map of average inter-ocular alignment for all data segments (159318 frames, n=3 animals) with overlay of isodensity contours from Figure 2H. **(J)** Map of average inter-ocular alignment as in J with left eye movements frozen.

263
264

265 al. 2018), torsional rotations in freely moving mice spanned a wide range of rotation angles (Figure 4 –

266 figure supplement 2A-D), and were correlated with head pitch (Pearson's correlation coefficient (r): detect

267 -0.72, 0.58, track: -0.60 and 0.53 for left and right eyes respectively, N=4406 detect and 13624 track

268 frames, N=3 mice, Figure 4 – figure supplement 2C-D) as well as head roll (Pearson's correlation coefficient

269 (r): detect: -0.46, -0.47 track: -0.45 and -0.48 for left and right eyes respectively, N=4406 detect and 13624

270 track frames, N=3 mice, Figure 4 – figure supplement 2 L-M), as found previously for freely moving rats

271 (Wallace, Greenberg et al. 2013). As with rats, the rotational relationship between the two eyes was

272 dynamic with different forms of coordination (Figure 4 – figure supplement 2E-I), including episodes of in-

273 and excyclovergence (torsional rotation of both eyes toward or away from the nose respectively) as well

274 as dextro- and levocycloversion (torsional rotation of both eyes to the animal's right or left

275 respectively).We next analyzed how effectively rotations of the eye around multiple rotational axes

276 combined to compensate the rotation of the head (Figure 4A, Figure 4 – figure supplement 3A-G). We

277 compared movement of the head around its rotational axes and eye movements around the same

278 rotational axes (Figure 4A), effectively defining alternative rotational axes for the eyes to match the axes

279 of the head. Rotation of the eye around these re-defined axes would involve simultaneous rotations in

280 multiple of the eye's anatomical axes. The gain of this compensation was relatively linear and less than

281 unity for both pitch- and roll-axes, indicating on average under-compensation of the head rotation (slope

282 (gain) of relation for pitch axis, -0.45±0.12 and -0.48±0.06; roll axis -0.51±0.12 and -0.62±0.05 for left and

283 right eye respectively, 168852 frames, N=3 mice). The relatively linear relationships between head and

284 eye rotation around the head pitch and roll axes (Figure 4B) with a transition through the origin suggests

285 that the horizontal, vertical and torsional eye movements are combined to effectively compensate pitch-

286 and roll-related head movements. We next digitally froze each individual eye rotation axis (torsion,

287 vertical and horizontal) and measured the effect on countering the head rotation (Figure 4C). For rotations

288 around the head x-axis (head pitch changes) the gain of compensation was most affected by freezing

289   torsional rotations (Figure 4C, gain mean±SD, control: -0.45±0.12and-0.48±0.06; torsion frozen -0.24±0.1

290   and-0.24±0.01, for left and right eyes respectively, N= 168852 frames, N=3 mice), while freezing vertical

291   or horizontal rotations had more minor effects (Figure 4C, Table 3). The gain of compensation for rotations

292   around the head y-axis (head roll changes) was dramatically affected by freezing vertical rotations (Figure

293   4C, gain mean±SD, control: -0.51±0.12and -0.62±0.05, vertical frozen -0.16±0.14and -0.17±0.03, for left

294   and right eyes respectively, N= 168852 frames, N=3 mice), with freezing torsion also reducing

295   compensation gain but to a lesser extent (Figure 4C, Table 3). We next quantified the stability and

296   alignment of the animal's binocular visual field during the pursuit sequences and determined the location

297   of the functional foci within the stabilized region.

298

Table 3. Compensation gain of eye rotations for head X or Y-axis rotations

Effect of digitally freezing torsional, vertical and horizontal eye rotations on the gain of compensation of X and Y head rotations. Data taken from 168852 frames, from 3 animals

Eye	Rotation direction	Rotation	All Rotations (mean ± SD)	Eye rotation frozen (mean ± SD)
Left	X	Torsion	-0.45±0.12	-0.24±0.1
		Horizontal	-0.45±0.12	-0.32±0.06
		Vertical	-0.45±0.12	-0.35 ±0.08
Right	X	Torsion	-0.48±0.06	-0.24±0.01
		Horizontal	-0.48±0.06	-0.36±0.08
		Vertical	-0.48±0.06	-0.34±0.03
Left	Y	Torsion	-0.51±0.12	-0.35±0.05
		Horizontal	-0.51±0.12	-0.51±0.11
		Vertical	-0.51±0.12	-0.16±0.14
Right	Y	Torsion	-0.62±0.05	-0.45±0.05
		Horizontal	-0.62±0.05	-0.62±0.02
		Vertical	-0.62±0.05	-0.17±0.03

321 **Functional foci are located in the motion-stabilized binocular visual field**

322 Similar to rats, left and right visual fields overlapped extensively (Hughes 1979, Drager and Olsen 1980),

323 with eye movements creating variability in the extent of the overlap at the edges of the two visual fields,

324 the transition from monocular to binocular (Figure 4D). The functional foci for both eyes were

325 predominately contained within the region of continuous binocular overlap. A horizontal transect through

326 the optical axis for all animals showed a gradual transition from continuous binocular coverage to zero

327 binocular coverage commencing just nasal of the optical axis (Figure 4D, Figure 4 - figure supplement 3H

328 and I), indicating that the region of highest RGC density spans this transitional region whereas the

329 functional foci are, on average, contained within the binocular region (Figure 4D - figure supplement 3H).

330 We next quantified the variability of alignment of the left and right visual fields within the binocular

331 region, and specifically in the functional focus location (Figure 4E) by using the center of mass (50%

332 isodensity contour center) of the left eye functional focus as an initial reference point and projecting this

333 point to the boundary of a hypothetical sphere surrounding the head. This contact point on the sphere

334 was then re-projected into the right eye to identify the matching location of the left eye (Figure 4E). We

335 then followed the trajectory of the re-projected point in the right eye to get a measurement of alignment

336 variability (Figure 4F, for comparison with the locations in the right eye projected into the left eye see

337 Figure 4 – figure supplement 3I-K). While pursuing crickets, alignment precision varied through time

338 (Figure 4G) with the mean alignment of the reference point over all animals and data segments being ~8-

339 9°, which is around the size of V1 cortical neuron receptive fields (~5-15° (Niell and Stryker 2008), Figure

340 4H, mean±SD, left eye projected into right eye 8.8±6.9°; right eye projected into left eye 8.6±6.7°).

341 Repeating this analysis for all points within the region where the probability of binocular overlap was

342 greater than 5% showed that there was a relatively uniform alignment over the entire region (Figure 4I),

343 and that the average alignment error in the functional foci was 8-10°. Coordination of eye movements

344 was important for alignment, as freezing the movements of one eye to its mean position resulted in a

345   significant increase in the alignment error when comparing individual cricket tracking sequences (left all

346   rotations vs. left eye frozen P=1.78x^{-10}, right eye all rotations vs. right eye frozen P=7.12x10^{-11}, N=52

347   sequences, unpaired Student's t-test), and a ~54% increase in the mean alignment error over all frames

348   for the reference location (Figure 4I, left eye projected into right eye (left eye frozen) 13.4±8.3°; Right eye

349   projected into left eye (right eye frozen) 13.4±8.3º, mean±SD, 159318 frames, N=3 mice), which also

350   resulted in a uniform increase in alignment error over the whole overlap region (Figure 4J and Figure 4 –

351   figure supplement 3J-L). In summary, during pursuit behavior the functional foci are located in a stable

352   binocular region of the mouse's visual field. However, in the absence of a mechanism for voluntarily

353   directing its gaze towards a specific target, such as smooth pursuit, tight coupling of VOR evoked eye

354   movements to head rotations would seem to be restrictive to an animal's ability to move the target into

355   a specific part of their visual field during pursuit. We therefore next measured what mechanisms mice use

356   to bring the prey into their functional focus.

357

358   **Behavioral mechanisms for maintaining prey within functional foci**

359   At detection, mice orient towards their target, aligning their head with the prey and running towards it

360   (Figure 2D), keeping the cricket within a narrow window around its forward direction. This provides a

361   direct way for mice to hold their prey within their binocular visual fields (Figure 4D). We next measured

362   whether additional head or eye movements are used to keep the target within the functional foci. If the

363   mice were actively maintaining the prey within a fixed location of their visual fields the position of the

364   cricket image should not change as the mouse approaches the cricket. The cricket image location could

365   be maintained by either a head or eye rotation. If they were not actively maintaining the prey in a fixed

366   location, the cricket images should shift downwards in the visual fields as the mouse approaches. To

367   distinguish between these two possibilities we plotted the cricket positions in the eye views color-coded

368   by the distance between the mouse and cricket (Figure 5A). As the mouse approached the cricket during

369   the track behavioral epoch, the projected cricket positions shifted lower in the visual field (Figure 5A

370   lower). This suggests that the mice did not use additional head or eye movements (Figure 5 – figure

371   supplement 1) to bring the cricket into the functional foci, but rather manipulated the cricket's position

372   in the eye view by orienting and moving towards the target. Consistent with this, head pitch remained

373   stable as the mice approached the crickets (Figure 5B). Furthermore, there was no significant difference

374   in head pitch as a function of distance to the cricket between non-tracking and tracking periods (non-

375   tracking head pitch: -3.7±26.5°, mean±SD, median = -11.3°, tracking head pitch: -12.9±15.7°, mean ± SD,

376   median = -14.6°, Ks test, P=0.709, paired Student's t-test P=0.197, N=18 detect-track sequences, N= 3

377   mice). In addition, and consistent with previous findings (Michaiel, Abe et al. 2020), mice did not

378   significantly converge their eyes as they approached the crickets (non-tracking head vergence: 7.6 ±13.5°,

379   mean±SD, median = 8.6°, tracking head vergence: 2.5 ±16.7°, mean ± SD, median = 3.2°. Ks test, P=0.425,

380   paired Student's t-test P=0.225, N=18 detect-track sequences N = 3 mice, Figure 5 – figure supplement 1J
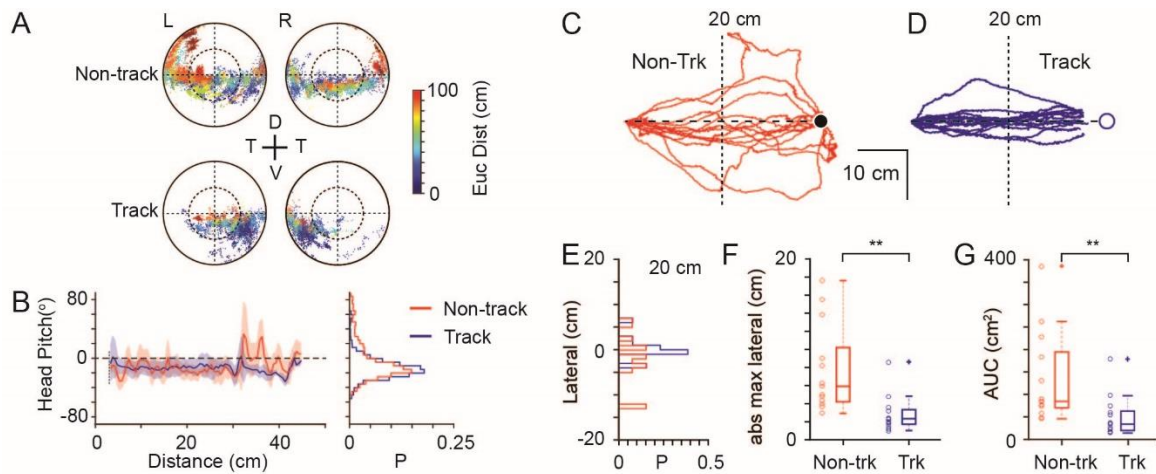
381

Figure 5 with 1 supplement
Mechanisms used to maintain prey within a focal visual region.
(A) Corneal locations of cricket position color-coded by Euclidean distance to cricket for non-track (upper) and track (lower) epochs (18 data sequences, 15649 non-tracking and 8510 tracking frames, n=3 animals). **(B)** Mean and SD head pitch with Euclidean distance to cricket (left) and distribution of head pitch angles (right) for non-track (red) and track (blue) epochs (datasets as in A). **(C)** Mouse trajectories during non-track epochs rotated and overlaid to show deviation from a direct path (13 trajectories from 3 animals). **(D)** Mouse trajectories as in D but during track epochs (13 trajectories from 3 animals). **(E)** Histogram of lateral deviations for non-track (red) and track (blue) data in C and D calculated 20 cm from the end of the trajectory. **(F)** Boxplots and individual data points of absolute maximal lateral deviation from a direct path between start and end points for non-track (red) and track (blue) epochs (datasets as in C & D), ** P=0.0006, Wilcoxon's Rank Sum Test. **(G)** Boxplots and individual data points of area under the curve (AUC) of mouse trajectories during non-track (red) and track (blue) epochs (datasets as in C & D),** P=0.0029, Wilcoxon's Rank Sum Test.

382
383

384 and Table 4). These observations suggest that the primary role for the eye movements is stabilizing the

385 visual fields.

386

387 **Table 4. Eye rotations during non-tracking and tracking periods**

388 Horizontal, vertical and torsional eye rotations during the non-tracking and tracking periods in Figure 5.
389 Data taken from 18 non-track epochs and 18 track epochs, from 3 animals.

Ocular Rotation	Non-Trk (mean ± SD) *(median)*	Track (mean ± SD) *(median)*	p value (KS)	P value (Student T-test)
Lt Horizontal	-1.8 ± 9.9º *(-1.7º)*	-1.8 ± 14.9º *(-3.5º)*	3.9×10^{-2}	0.162
Lt Vertical	0.8 ± 11.2º *(-0.4º)*	4.5 ± 11.1º *(4.9º)*	0.425	0.616
Lt Torsional	2.9±16.1º *(0.0º)*	1.3±20.6º *(0.0º)*	0.945	0.610
Rt Horizontal	5.7 ± 10.9º *(5.5º)*	1.0 ± 9.9º *(1.7º)*	9.82×10^{-2}	1.08×10^{-2}
Rt Vertical	-3.6±13.4º *(-6.3º)*	5.6±12.7º *(-7.1º)*	0.945	0.804
Rt Torsional	0.32±13.5º *(0.0º)*	0.7±12.3º *(0.0º)*	0.425	0.366

390

391
392

393

394
395

396   If mice successfully track and capture prey by retaining the target in front of them, then this should be

397   reflected in the trajectories taken by the mice during the tracking epoch compared to the non-tracking

398   behavioral epochs. During cricket tracking periods, mice ran directly towards the cricket, and their

399   trajectories were significantly straighter than during equivalent non-tracking phases (Figures 5C-G).

400   Lateral deviation at the half-way point (Figure 5E, non-tracking 4.3±4.0 cm, tracking 1.4±2.0 cm, P=0.009),

401   maximum lateral deviation (Figure 5F, non-tracking, 7.7±4.9 cm, tracking 2.8 ±2.0 cm, P=0.0006) and the

402   area between the trajectory and minimum distance path to the target (Figure 5G, area under the curve,

403   non-tracking 135.6±102.7 cm^2, tracking 51.3±45.8 cm^2, P=0.0029) were all significantly smaller in the

404   tracking epochs (all comparisons mean±SD, N=13 tracking and non-tracking sequences, N=3 mice,

405   Wilcoxon's Rank Sum Test).

406   Together this suggests that mice do not make compensatory vertical head movements, tracking eye

407   movements or vergence eye movements to keep prey within their functional foci but instead retain their

408   target within a restricted bearing by running straight towards it. This raised the question of what

409   advantage is this behavior to the mouse and what is unique about the functional focus position on the

410   cornea?

411   **Functional foci are located in region of minimized optic flow**

412   Optic flow is the pattern of object motion across the retina that can be self-induced, through eye, head or

413   translational motion, or induced by motion of objects in the environment, or combinations thereof (for

414   review see: (Angelaki and Hess 2005). In a freely moving animal in a still environment, translational motion

415   results in a pattern of optic flow that consists of a radial flow-fields emanating from a point of zero-velocity

416   (Figure 6A). While optic flow is used by many species for both navigation and the estimation of the motion
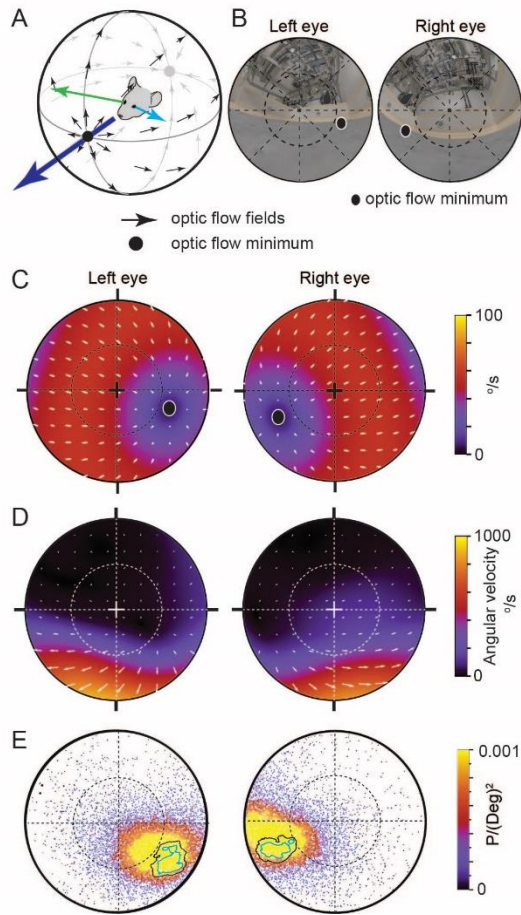
417

Figure 6
Functional foci are located in the regions of reduced optic flow during forward motion.
(A) Schematic of idealized optic flow (black arrows) as a mouse translates forwards (after (Sabbah, Gemmer et al. 2017)). Left (blue arrow) and right (green arrow) gaze vectors. **(B)** Location of optic flow minima in reconstructed mouse eye views of the cricket and experiment arena (from Figure 1H), circle represents 45°. **(C)** Optic flow map in corneal views, showing flow velocity (color coding) and direction (white arrows) calculated for the idealized spherical environment in 6A with forward motion of 50 cm/s. **(D)** Optic flow maps in corneal views during track epochs (5269 frames), from one animal. **(E)** Probability density map of optic flow poles in mouse corneal views during track epochs (data as in Figure 2G, 13641 frames), with overlay of isodensity contours from Figure 2H.

418
419

420

421   properties of moving objects, motion induced blur degrades image formation on the retina and decreases

422   resolution depending on the animal's direction of travel (Land 1999). Optic flow is minimized in the

423   direction of travel directly in front of the animal (Sabbah, Gemmer et al. 2017), with flow fields directed

424   away from travel direction and forming a second minimum directly behind the animal's head (Figure 6A,

425   see also (Angelaki and Hess 2005).To measure the characteristics of optic flow in in both eyes of freely

426   moving mice and to relate this flow pattern to the location of the functional foci, we next calculated

427   average optic flow from freely moving data during pursuit behavior using the digitized environment and

428   eye-views (Figure 6B). First, we calculated optic flow in the idealized case of forward translation motion

429   when all surrounding surfaces were equidistant (Figure 6C). As mice have laterally facing eyes (optical axis

430   = 59.9±19.8° and -62.3±14.7° lateral of frontal for the left and right eyes respectively, N=3 mice), idealized

431   forward motion resulted in the region of minimal optic flow in each eye being located off optical axis in

432   the ventro-medial corneal region representing the animal's forward direction (radial displacement from

433   optical axis 36.64±0.92° and -41.11±2.27°, rotational angle 122.95±17.05° and -107.94±9.96°, for the left

434   and right eyes respectively, mean ± SD, N=2 mice, Figure 6C). During free movement both the distance

435   from the eyes to objects in the environment, as well as head and eye-rotations had a strong influence on

436   the optic flow fields. We visualized the average flow fields during free motion by calculating the optic flow

437   on the cornea during multiple pursuit trials (N=20 prey chases containing 52 tracking sequences, initial

438   Euclidean distance mouse-cricket >20 cm). The resulting optic flow density maps were complex with a

439   wide range of average speeds (133.44±221.42 °/s, mean±1SD, median 28.64 °/s, interquartile range 4.57–

440   137.18 °/s, N=2 mice, Figure 6D). The area of lowest optic flow extended from nasal field of view to

441   overhead (Figure 6D) but unlike the simulated case (Figure 6C) optic flow was not symmetric around the

442   regions of minimal optic flow. Optic flow in the 30x30° region surrounding the ventro-medial point of

443   minimal optic flow was significantly lower than that in an equivalent region in the ventro-temporal region

444   during free movement, but not in the simulated case (free movement: nasal 46.3±9.8 °/s, temporal:

445   199.4±29.0 °/s, P=0.0014, simulated: nasal 163.6±82.2 °/s, temporal: 833.0±416.5 °/s, P=0.0662,

446   mean±SD, two-sided t-test, unequal variance, N=2 mice). Optic flow was higher in the lower visual field

447   and considerably lower in the upper visual field (lower left eye visual field: 262.44±106.50 °/s, upper left

448   eye visual field: 44.87±24.31 °/s, P=1.78x10^{-20}, lower right eye visual field: 361.91±168.80 °/s, upper right

449   eye visual field: 40.59±22.79 °/s, P=6.68x10^{-19}, Two-sided t-test, unequal variance, N=2 mice), due to the

450   greater distance between ceiling and mouse (distance to floor 2±1cm, distance to ceiling 308±107cm,

451   9873 frames, N=3 mice). Given the advantage of low optic flow to mammalian vision, we next quantified

452   the position of least optic flow during prey tracking. We calculated the location of the translational optic

453   flow minimum in each frame for each eye, and created a probability map of this location over the visual

454   field (Figure 6E). The region of highest likelihood for the presence of the optic flow minimum overlapped

455   considerably with the functional foci in both eyes during the tracking epochs of the pursuit behavior

456   (overlap of optic flow 95% minima and functional foci 50% regions: 100% and 99±1%, overlap of optic flow

457   50% minima and functional foci 50 % regions: 61±14 % and 72±4 % in left and right eyes respectively, N=3

458   mice, Figure 6E). Together this shows that mice preferentially maintain their prey in the region of reduced

459   optic flow during pursuit, where the retinal image of their prey is least distorted due to motion induced

460   image blur.

Discussion:

461

462   We developed a technique for reconstructing the visual fields in a freely moving mouse during prey pursuit

463   to quantify the spatial relationship between the environment, cricket and the mouse. Using this approach,

464   we show that mice, while pursuing crickets, preferentially maintain the prey in a localized region of their

465   visual field, termed here the functional focus. The positional maintenance of the cricket was not achieved

466   by active eye movements that followed the prey, but rather by the animal's change in behavior,

467   specifically the head-movement and orientation towards the prey during pursuit. While eye rotations

468   stabilized the visual field via the vestibulo-ocular reflex by countering head rotations, the rotations were

469   not specific to either prey detection or prey tracking. This strongly suggested that eye-rotations in mice,

470   like in rats, primarily stabilize their large field of view and that all three rotational axes, including ocular

471   torsion, combine to counter head rotations. In addition, we also show that eye rotations cannot be

472   predicted from head rotations in any one axis as has been suggested by recent studies of mouse eye

473   motion (Meyer, Poort et al. 2018, Meyer, O'Keefe et al. 2020, Michaiel, Abe et al. 2020) but rather by a

474   combination of all head rotations (Figure 4 – figure supplement 2). As the eye rotations were

475   predominately associated with countering head-rotations, this raised the question of whether the mouse

476   can use a large fraction of its stabilized visual field to pursuit crickets, or whether a specific region is

477   utilized. To accurately determine the correspondence between the animal's visual field and the retinal

478   image, we developed a quantitative model of the mouse eye and optics. Using this, we show that the

479   location of the functional focus does not coincide with the retinal region with the highest total density of

480   retinal ganglion cells that are laterally facing, but rather the highest density of Alpha-ON sustained RGCs,

481   whose general properties have been previously proposed to be well suited for this purpose (Bleckert,

482   Schwartz et al. 2014). Finally, we used the detailed, digitally rendered reconstruction of the arena and

483   surrounding room to calculate the realistic optic flow in the visual fields (Gibson, Olum et al. 1955, Sabbah,

484   Gemmer et al. 2017, Saleem 2020) of the mice as they pursued crickets, which showed that the functional

485   foci coincide with the region of the visual fields with minimal optic flow during the cricket pursuit, and

486   presumably are thereby minimally distorted by motion-induced image blur (for review see (Angelaki and

487   Hess 2005)). Critical to this finding was the ability to isolate the visual sense, generate both a detailed

488   reconstruction of both the local environment and the animal's ocular anatomy and optical pathways, but

489   also record eye motion in all three optical axes especially ocular torsion, something that has only been

490   achieved in rats (Wallace, Greenberg et al. 2013).Lastly, by building an optical model and establishing the

491   relationship between the retinal surface and the corneal surface we were able to relate the data

492   generated from published studies on retinal anatomy (Drager and Olsen 1981, Sterratt, Lyngholm et al.

493   2013, Bleckert, Schwartz et al. 2014) and physiology (Pang, Gao et al. 2003, Murphy and Rieke 2006, van

494   Wyk, Wassle et al. 2009, Dhande, Stafford et al. 2015, Martersteck, Hirokawa et al. 2017, Sabbah, Gemmer

495   et al. 2017) to our behavioral data.

496   Both estimates of the field of view of the mouse eye (Drager 1978) and electrophysiological

497   measurements of receptive field locations of visually responsive neurons (Drager and Olsen 1980, Wagor,

498   Mangini et al. 1980) have established that the binocular region of the visual field in mice is contained

499   within the nasal visual field of each eye, and spans a region of 30-40° in front of the animal (Wagor,

500   Mangini et al. 1980). We present here, that similar to the rat (Wallace, Greenberg et al. 2013), the

501   overlapping monocular fields that make up the binocular overlap are not constantly maintained (Figure

502   4H) but fluctuate at the margins as the eyes rotate to counter head rotations (Figure 4D), resulting in a

503   region where there is a transition from one area with near continuous binocular coverage, through to a

504   region that is invariably monocular. The functional focus described here lies within the region of high

505   probability of maintained binocular overlap. This region of the visual field projects onto the temporal

506   retina, which contains both ipsilaterally projecting (uncrossed) RGCs (Drager and Olsen 1980, Reese and

507   Cowey 1986) and RGCs which form part of the callosal projection pathway (Olavarria and van Sluyters

508   1983, Laing, Turecek et al. 2015, Ramachandra, Pawlak et al. 2020), both of which are considered central

509   to binocular visual processing. In addition, the current study adds to the significance to these previous

510   findings and suggests that the functional focus location is well placed to support stereoscopic depth

511   perception, assuming that this form of visual processing is available to and employed by the mouse (Scholl,

512   Burge et al. 2013, Scholl, Pattadkal et al. 2015, La Chioma, Bonhoeffer et al. 2019, Samonds, Choi et al.

513   2019, La Chioma, Bonhoeffer et al. 2020). In addition, while the overall highest density of retinal ganglion

514   cells in mice is located in the region around the optical axis (Drager and Olsen 1981), a recent study

515   examining the distributions of various different subclasses of RGCs has shown that the highest density of

516   Alpha-ON sustained RGCs resides in the superior-temporal retina (Bleckert, Schwartz et al. 2014) in a

517   region which would approximately coincide with the functional focus. These Alpha-ON sustained RGCs

518   have center-surround receptive fields, a rapid response and fast conducting axon, and are thought to be

519   "spot detectors" (for review see (Dhande, Stafford et al. 2015)). In addition, the Alpha-ON sustained RGCs

520   in this particular retinal region differ from the same RGC-type in other regions of the retina as they have

521   a significantly smaller dendritic tree radius and subtend a smaller area of physical space as well as have

522   overlapping receptive fields (Bleckert, Schwartz et al. 2014). Taken together, the cellular properties as

523   well as the region in-front of the animal which provides their input are consistent with the requirements

524   for tracking small and mobile targets (Lettvin, Maturana et al. 1959, Dean, Redgrave et al. 1989, Bleckert,

525   Schwartz et al. 2014, Procacci, Allen et al. 2020). A recent study has shown that both wide-field and

526   narrow-field neuronal types in the mouse superior colliculus play central roles in the detection and pursuit

527   phases of this pursuit task respectively (Hoy, Bishop et al. 2019), and consistent with this, Alpha-ON

528   sustained RGCs having projections to the superior colliculus (Martersteck, Hirokawa et al. 2017). It is

529   currently unclear how the primary visual cortex (V1) contributes to this behavior, but some role is possible

530   if not probable, which would also be supported by the strong Alpha RGC projection to the dorsal lateral

531   geniculate nucleus and thus V1 (Martersteck, Hirokawa et al. 2017). Additionally, an increased cortical

532   magnification factor occurs in the region corresponding to the nasal, binocular visual field (Schuett,

533   Bonhoeffer et al. 2002, Garrett, Nauhaus et al. 2014).

534   Finally, we show that the region that contains these Alpha-ON sustained RGCs also coincides with the

535   region of minimum optic flow and therefore reduced image blur during translation pursuit, a feature

536   which would supports accurate localization of small targets by Alpha-ON sustained RGCs. Patterns of optic

537   flow are thought to be an important component of perception of self-motion (Lappe, Bremmer et al.

538   1999). Mechanistically supporting this, global alignment across the retina of the preferred orientation of

539   direction-selective retinal ganglion cells with the cardinal directions of optic flow during idealized motion

540   has been shown in mice (Sabbah, Gemmer et al. 2017). The average optic flow measured here was,

541   perhaps not surprisingly, strikingly different from that observed with idealized motion, resulting in large

542   part from the large differences to objects in the environment in which the behaviors were performed. For

543   fast moving, ground dwelling animals like mice, considerable asymmetry in optic flow across the visual

544   field may be the more normal case, considering that objects above the animal are, in general, likely to be

545   more distant.

546   In freely moving rats it has been shown that ocular torsion is correlated with head pitch such that nose-

547   up rotation of the head is counteracted by incyclotorsion (rotation towards the nose) of both eyes, with

548   nose-down pitch counteracted by excyclotorsion (Wallace, Greenberg et al. 2013). These rotations have

549   the effect of stabilizing the horizontal plane of the retina with respect to the horizon. The considerable

550   radial separation between the optical axis of the eye and both the functional foci observed in the current

551   study as well as the highest density region of Alpha-ON sustained RGCs (Bleckert, Schwartz et al. 2014)

552   renders the direction in which these regions point highly sensitive to torsional rotation. Consequently,

553   torsional rotation also has an important effect on alignment of the left and right visual fields in addition

554   to its role in visual field stabilization. We show here that torsional rotation in freely moving mice is also

555   dynamic, with episodes showing in- and excyclovergence as well as dextro- and levocycloversion. Further,

556   while the correlation between torsional rotation and head pitch observed in rats was measured, there

557   was also an additional relation between ocular torsion and head roll consistent with VOR-evoked dextro-

558   and levocycloversion. Consequently, prediction of torsion using a model based on head pitch alone

559   resulted in an average error of around 7°, while an expanded model including roll as well performed better

560   (Figure 4 – figure supplement 2J-O).

561   In summary, we show here that during pursuit mice preferentially keep their intended prey in a localized

562   region of their visual fields, referred to here as the functional focus, but do so by orientating their head

563   and body and running directly towards the prey rather than with specific eye movements. The location of

564   the functional focus is within the binocular visual field, but in addition also coincides with the region of

565   minimal optic flow during the pursuit, and presumably also minimally distorted by motion blur.

566
567

568 **Methods:**

569 *Animal details*

570 Experiments were carried out in accordance with protocols approved by the local animal welfare

571 authorities (Landesamt für Natur Umwelt und Verbraucherschutz, Nordrhein-Westfalen, Germany).

572 Experiments were carried out using male C57/BL6JCrl mice (acquired from Charles River Laboratories).

573 At the time of the cricket hunting experiments, mice (n=9) were between 2-8 months old, and weighed

574 between 21-29g. Mice were maintained on a 12 hr light/dark cycle. Crickets (*Acheta domesticus*, Bugs-

575 International, Germany) were housed in 480x375x210 cm cages with *ad lib* water and food (powdered

576 mouse chow). Cricket body sizes ranged from 1 cm to 2 cm (1.8 ± 0.3 cm, mean ± SD, n=25).

577

578 *Implant surgery*

579 Animals were anaesthetized using fentanyl, medetomidine and midazolam (respectively 50µg/kg, 5mg/kg

580 and 0.5mg/kg, delivered i.p.), and analgesia was provided with carprofen (7mg/kg delivered s.c.). Body

581 temperature was maintained using a thermostatically regulated heating pad. Respiration rate and depth

582 of anesthesia was monitored throughout the procedure. Following opening of the skin and removal of

583 connective tissue overlying the sagittal suture and parietal bones, the skull was cleaned with H_2O_2 (3%). A

584 custom-made implant, consisting of a flat circular attachment surface for attachment to the skull, and

585 implant body with three anti-rotation pins and a magnet (Figure 7A-B), was fixed to the dried skull using

586 a UV-curing dental adhesive (Optibond FL, Kerr Corporation, Orange, California, USA) and a UV-curing

587 dental composite (Charisma, Kulzer GmbH, Hanau, Germany). The implant attachment surface and body

588 were made from light-weight, bio-compatible dental resin (Dental SG, Formlabs, Germany). Skin margins

589 were closed with 5/0 Vicryl sutures (Ethicon Inc, Somerville, NJ, USA) and a cyanoacrylate adhesive

590 (Histoacryl, B.Braun, Melsungen, Germany). The injectable anesthetic combination was antagonized with

591   naloxone, atipamezole and flumazenil (respectively 1.2mg/kg, 0.5mg/kg and 0.75mg/kg, delivered i.p.),
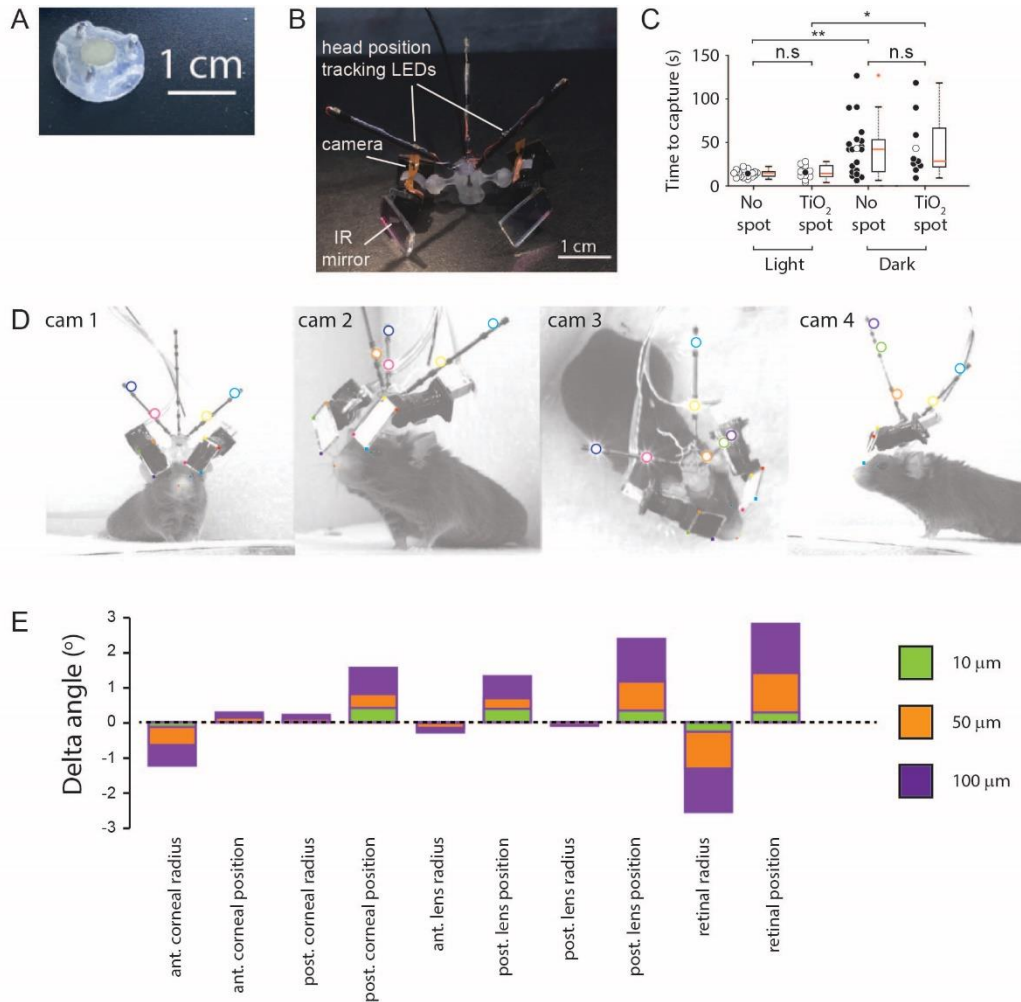
592   and the animal was allowed to recover.

Figure 7. Methods.
(A) Implanted baseplate with magnetic attachment point and restraining pin holes. **(B)** Miniaturized eye cameras and head position tracking system. Infrared illumination LEDs were mounted on the camera objective and reflected onto the eye using an IR-reflective mirror. Head position tracking IR-LEDs were mounted on three carbon-fiber struts attached to the head-mount. **(C)** Cricket capture times in lit or dark conditions in mice without (n=19 pursuit sequences, n=6 mice) or with (n=10 pursuit sequences in lit conditions and n=9 pursuit sequences in the dark, n=3 mice) corneal TiO2 torsion tracking spots, Lit vs Dark with no spot, P=0.0012, Lit vs Dark TiO2 spot, P=0.0133, Lit without spot vs Lit with TiO2 spot, P=0.69, Dark without spot vs Dark with TiO2 spot, P=1. n.s. = non-significant, *P<0.05, **P<0.01. Paired Wilcoxon's signed rank tests. For these experiments, pursuits were conducted in a smaller arena (480 x 375 x 210 cm). **(D)** Images of mouse with eye camera and head position tracking system for anatomical calibration. Head mount and anatomical features marked. Anatomical features: Left (blue filled circles) and right (green filled circle) medial canthi, left (orange filled circles) and right (red filled circle) nostril positions. Head mount features: position tracking LEDs (large colored circles), IR mirror corner positions (small colored filled squares). **(E)** Sensitivity of the radial elevation on the retina in the mouse eye model to changes in the radii of curvature and thicknesses of the model optical components.

594   *Positioning of the head-mounted cameras*

595   The eye cameras for oculo-videography were mounted on mounting arms which were attached to a

596   baseplate with complementary holes to the anti-rotation pins on the implant and fitted with a magnet of

597   complementary polarity. During positioning of the head-camera, mice were anaesthetized with isoflurane

598   (induction: 3-5% isoflurane, maintenance: 2.0% isoflurane in air). Anesthetic depth and body temperature

599   were monitored as above. The cameras were positioned to have a sharp image of the entire eye, with the

600   mounting arms adjusted such that the cameras and mounting system caused minimal disruption to the

601   mouse's lateral and frontal field of view. Mounting arms were secured with cyanoacrylate adhesive glue

602   (Histoacryl, B.Braun, Melsungen, Germany). The eye-camera system was then removed and the animal

603   allowed to recover.

604

605   *Training procedure*

606   Mice were acclimated to cricket capture in their home cage. Individual crickets were placed in the mouse's

607   home cage overnight, in addition to their standard *ad lib* mouse food. Mice were handled and habituated

608   to the experimenter, the head cameras, and the head tracking mounts. The ability of each mouse to

609   visually track the crickets was assessed using the protocol of Hoy et al.(Hoy, Yavorska et al. 2016). Briefly,

610   the ability of the mice to track and capture crickets in a white walled, 480 x 375 x 210 cm arena was

611   assessed in lit and dark conditions (Figure 7C). Mice were given 2 minutes in which to capture the crickets.

612   Prior to the assessment mice were food deprived overnight before the trial.

613   *Placement of torsion tracking marks*

614   Crenellations along the iridial-pupil border were less distinct in mice than those previous described in rats

615   (Wallace, Greenberg et al. 2013). Ocular torsion changes were therefore measured by tracking the

616   rotations of small spots of titanium dioxide (TiO$_2$) paste dots (~ 300 μm) applied to ventral and/or

617   temporal locations on the cornea as described in (van Alphen, Winkelman et al. 2010). The TiO$_2$ paste

618   consisted of TiO$_2$ powder (Kronos Titan GmBH, Leverkusen, Germany) mixed with a small quantity of

619   sterile Ringer's solution. Application of the TiO$_2$ spots was performed with the animal anaesthetized with

620   isoflurane (induction: 5% isoflurane, maintenance: 0.5-1.0% isoflurane in air, total time anesthetized 5-

621   10mins). Anaesthetic depth and body temperature was monitored as above. Following application of TiO$_2$

622   spots, mice were allowed to recover for >45 minutes prior to a cricket hunt. The presence of the TiO$_2$

623   marks did not significantly change the animal's cricket hunting performance as assessed by the average

624   time taken to capture crickets (Figure 7C).

625

626   *Experiment procedure*

627   Initially, mice were allowed to explore the experimental arena (1x1x0.26 m) without head camera mounts.

628   During subsequent training sessions mice were acclimated to cricket hunting, with the head cameras on,

629   in the experiment arena. Auditory white noise (60-65 dB, NCH-Tone generator v 3.26, NCH Software, Inc.

630   Greenwood Village, USA) was provided through 4 speakers (Visaton, Germany), one on each wall of the

631   arena. Olfactory noise was provided by ventilating the arena (TD-1000/200 Silent fan, S&P, Barcelona,

632   Spain) through a perforated floor (5cm perforation spacing) with air blown through a cage containing live

633   crickets (cricket cage dimensions 480x375x210cm). During experiments the arena was lit by a single lamp

634   (4000 K, 9W, Osram, Munich, Germany) positioned ~1m above the arena. During each experiment the

635   mouse was given 5 minutes to explore the arena without head cameras. After this period the mouse was

636   removed from the arena and the head cameras were mounted. At the commencement of each hunt the

637   cricket was released at a variable location into the central region of the arena.

638

639   *Eye camera and head position tracking system*

640   Head and eye tracking was performed as described in (Wallace, Greenberg et al. 2013), with modifications

641   as described below. The eye camera mount and implant were re-designed to be smaller, lighter and

642   stronger (Figure 7A-B). The camera system body, camera holders and mounting arms were produced using

643   a Formlabs Form2 SLA 3D printer (Formlabs Inc., USA), with Dental SG Resin (Formlabs Inc., USA) as the

644   primary construction material. The cable used for data transfer and camera and position tracking LEDs

645   power inputs was a flat flexible printed circuit (Axon Kabel GmbH, Leonberg, Germany). Eye movements

646   were recorded at 60 Hz (camera resolution 752x480 pixels), with illumination provided by a ring of three

647   IR-LEDs (λ=850 nm, OSRAM SFH4050 or SFH4053 @ 70mA, RS Components, Germany) surrounding the

648   camera lens. The mouse's head position and head rotations were tracked using seven IR-LEDs (λ = 950

649   nm, OSRAM SFH4043 @ 70mA, RS Components, Germany) mounted on three struts of carbon fiber that

650   projected from the body of the camera system. The resultant total system weight was ~3g, including

651   effective cable weight.

652

653   *Mouse head and cricket position tracking*

654   The positions of the cricket within the arena were recorded using 4 cameras (488 x 648 px, recorded at

655   200 Hz, piA640-210gm, Basler cameras, Basler Ahrensburg, Germany) fitted with NIR-blocking filters

656   (Calflex X, Qioptiq, Germany). Cameras were located ~1.5 m above the arena, and were positioned so that

657   the arena was covered at all points by 2 or more cameras from differing vantage points. Mouse IR-head

658   tracking LEDs were recorded at 200 Hz using 4 cameras (piA640-210gm, Basler cameras, Basler

659   Ahrensburg, Germany). Image acquisition, synchronization and mouse head rotation calculations were

660   performed as described previously (Wallace, Greenberg et al. 2013).

661

662   *Anatomical model*

663   Head mount features and mouse anatomical features (medial canthi and nostril positions) were recorded

664   at 50 Hz using four synchronized cameras (acA2040-90 um, Basler cameras, Basler Ahrensburg, Germany)

665   fitted with 25 mm focal length objectives (CCTV lens, Kowa Optical Products Co. Ltd, Japan) calibrated as

666   described for the overhead cameras in (Wallace, Greenberg et al. 2013). Cameras were positioned to

667   provide images of the animal and headset from different angles to allow triangulation of the anatomical

668   features (Figure 7D). During acquisition of the calibration images, the animal was illuminated with 12 IR-

669   LED modules, (λ = 850, Oslon Black PowerStar IR-LED module, ILH-IO01-85ML-SC201_WIR200, i-led.co.uk,

670   Berkshire, UK) run at 1A. Position tracking LED, medial canthi, nares, mirror corner and camera chip corner

671   positions were marked in 2 or more camera views, in multiple synchronized frames. Based on the

672   triangulated positions of anatomical features, head cameras and position tracking LEDs the mouse's eye

673   position could be placed a common coordinate system.

674   To establish the animal's horizontal plane from the head tracking LEDs, a position for the animal's nose

675   was first defined by averaging to 3D positions of the marked nostrils. A pre-forward vector was calculated

676   using the direction between mean of eyes and nose and a pre-up vector as vector orthogonal to the pre-

677   forward and vector between the eyes. Next, the left vector was defined as orthogonal to pre-forward and

678   pre-up. Finally, the system was rotated by 40° around the left vector such that forward vector was

679   elevated. This established a head-fixed forward-left-up coordinate system that was based on the bregma-

680   lambda sagittal plane by tilting the eyes-nose plane by an angle of 40°.

681   *Interpolation*

682   Head tracking frame rates were 200Hz, while eye tracking cameras recorded at 60 Hz. Eye positions

683   were consequently interpolated as follows: Let

684    $$R_{t1}, R_{t2} \in SO(3)$$

685   be two rotations that transform the vector $(0,0,-1)^t$ into the gaze vectors v_{t1}, v_{t2} in head fixed

686   coordinates at times $t1$, $t2$. Then for a time t' with

687     $$t' = t1 + s * (t2 - t1) , 0 < s < 1$$

688   the corresponding rotation $R_{t'}$ is interpolated such that $v_{t'}$ is placed on the geodesic defined by v_{t1}, v_{t2}

689   with an angle of $s * \angle (v_{t1}, v_{t2})$ to v_{t1}, and the rotation of a vector perpendicular to $(0,0,-1)^t$ is

690   continuous and uniform between $t1$ and $t2$.

691

692   *Camera calibration*

693   Overhead cameras for animal position and pose tracking, tracking of crickets and the cameras used for

694   generation of the anatomical model were calibrated as described for the overhead cameras in (Wallace,

695   Greenberg et al. 2013) and the eye camera calibration performed as described in (Wallace, Greenberg et

696   al. 2013).

697

698   *Pupil position and pupil torsion tracking*

699   Pupil boundary tracking, compensation for eye image displacement, and gaze vector calculation was

700   performed as described previously in (Wallace, Greenberg et al. 2013). Where contrast between pupil and

701   iris was insufficient to allow automated pupil position tracking, pupil positions were manually tracked.

702   The TiO_2 spots for tracking ocular torsion were tracked manually in each image frame. Torsional rotations

703   were determined based on the tracked TiO_2 spot positions as follows. Total rotation of the eye was defined

704   as previously described in (Wallace, Greenberg et al. 2013), as:

705     $$R_{eye} = R_\phi R_\theta R_\psi$$

706
$$= \begin{bmatrix} 1 & 0 & 0 \\ 0 & \cos\phi & -\sin\phi \\ 0 & \sin\phi & \cos\phi \end{bmatrix} \begin{bmatrix} \cos\theta & 0 & -\sin\theta \\ 0 & 1 & 0 \\ \sin\theta & 0 & \cos\theta \end{bmatrix} \begin{bmatrix} \cos\psi & -\sin\psi & 0 \\ \sin\psi & \cos\psi & 0 \\ 0 & 0 & 1 \end{bmatrix}$$

707 where ϕ=vertical, θ=horizontal and ψ=torsional rotations. The mouse's gaze vector has the coordinates

708 $[0 \quad 0 \quad -1]^T$ for the reference position of the eye, and in each frame:

709
$$v^{gaze} = R_{eye} \begin{bmatrix} 0 \\ 0 \\ -1 \end{bmatrix}$$

710

711 With the eye in its reference position, we assume that the marked TiO_2 spot is located in the x-y plane of

712 the eye camera (Wallace, Greenberg et al. 2013). The anatomical location of this marked spot can then

713 be described by two unknown parameters r (where r>1 is the 3D distance of the eyeball surface to the

714 eyeball center, and a distance of 1 describes the rotation radius of the pupil) and α is the fixed angle

715 between the TiO_2 mark and the gaze vector. After eye rotation the 3D location of the TiO_2 is:

716
$$v^{mark} = R_{eye} \begin{bmatrix} r\,\sin\alpha \\ 0 \\ -r\,\cos\alpha \end{bmatrix}$$

717 and the predicted pixel coordinates of the spot in the image are:

718
$$\hat{p}^{mark} = \begin{bmatrix} a_{EC} \\ b_{EC} \end{bmatrix} + \frac{f}{z_0} \begin{bmatrix} v_1^{mark} \\ v_2^{mark} \end{bmatrix}$$

719 where a_{EC} and b_{EC} are the location in the image of the center of the eye ball and $\frac{f}{z_0}$ a scaling

720 factor, both of which are determined in the calibration procedure for pupil boundary tracking, described

721 in full in (Wallace, Greenberg et al. 2013).

722 When r and α are known the value ψ can be determined. Using the Matlab function **fminbnd** the squared

723 2D distance

724
$$|\hat{p}^{mark} \quad p^{mark}|_2^2$$

725   between the predicted and marked locations of the TiO_2 mark is minimized.

726   This method is used to determine the ocular torsion based on the TiO_2 spot location, both during and after

727   calibration. Calibration was performed as follows:

728   For a given r and α choice, ψ can be calculated as above. The sum of square errors in pixel locations is

729   then calculated over all frames. We optimized over r and α using the Matlab function **fminsearch**. To

730   initialize r, we make use of the fact that the pupil model, p^{mark} and r together determine the 3D location

731   of the mark v^{mark} in each image. For each frame we first calculated:

732

733
$$\Delta a = \frac{p_1^{mark} - a_{EC}}{f/z_0}$$

734

735
$$\Delta b = \frac{p_2^{mark} - b_{EC}}{f/z_0}$$

736

737
$$m = \min\left(1, \frac{r}{\sqrt{\Delta a^2 + \Delta b^2}}\right)$$

738

739
$$v_{init}^{mark} = \begin{bmatrix} m\Delta a \\ m\Delta b \\ -\sqrt{r^2 - m^2 (\Delta a^2 + \Delta b^2)} \end{bmatrix}$$

740

741
$$\alpha_{init} = \cos^{-1}\left(v^{gaze} \cdot v_{init}^{mark}/r\right)$$

742 Using this method α_{init} is estimated separately for each frame, and if the choice of r is correct then these

743 values should agree. We can use **fminbind** to minimize the following with respect to r:

744

745
$$\text{Var}(\alpha_{init}) = \overline{(\alpha_{init} - \overline{\alpha_{init}})^2}$$

746 After r is initialized, α_{init} is calculated, with α initialized using the mean over frames.

747 Torsional rotations were normalized by calculating a mean torsion value for the 0.01 % of frames that

748 were closest to both median pitch and roll of the head. Torsional values in other tracked frames were then

749 normalized to this mean torsion value.

750

751 *Cricket Position Tracking*

752 Cricket body positions were automatically tracked using the method and algorithm described for tracking

753 eye corners, as described in the section "*Compensation for lateral eyeball displacement – tracking of*

754 *anatomical landmarks around the eye*" in (Wallace, Greenberg et al. 2013). To increase the contrast

755 between the region around the cricket in the image and the cricket, ~100 background image frames (in

756 which neither mouse nor cricket was present) were averaged and subtracted from frames in which the

757 cricket was present. In frames where automated cricket position tracking was not possible, frames were

758 tracked manually. As the cameras used for cricket tracking had been calibrated along with the animal

759 position tracking cameras (see above), the 3-dimensional location of the cricket could be triangulated in

760 a common coordinate system with the animal's position.

761

762   *Classification of behavioral periods*

763   To decrease the effects of tracking noise and rapid head rotations, mouse velocity, target bearing and

764   inter-animal Euclidean distances were first filtered using a 50ms sliding window Gaussian filter.

765   The criteria used to classify the different hunt phases were based on those described in (Hoy, Yavorska et

766   al. 2016). In an initial step, behavioral end points (t_{end}) for capture periods were identified by manual

767   inspection of the tracking movies. Further identification of the behavioral start points (t_{start}) and t_{end} points

768   for the different hunt sequence epochs were then identified as described below.

769   The t_{end} points were defined as:

770   A. The t_{end} point for a detect period was defined as the last frame before (1) Mouse head velocity

771   in the direction of the cricket was >= 20 cm/s, (2) The mouse's bearing towards the cricket was constantly

772   below 90° and (3) the Euclidean distance between the mouse and cricket was continuously decreasing.

773   B. The t_{end} point for a tracking period was identified by locating local minima in the mouse-cricket

774   Euclidean distance time plots, where local minima were defined as points at which the mouse came within

775   a contact distance of 6 cm (measured from the tracked point on the mouse's head, giving a > 3 cm

776   separation between the mouse's nose and the cricket). These were followed either by a capture period

777   (see below) or were followed by a $\geqslant$ 5cm increase in inter-animal Euclidean distance, which were defined

778   as cricket escapes. In cases where the absolute value of the target bearing was > 90° before the mouse

779   turned towards the prey, the start of the tracking period was taken as the first frame in which the bearing

780   to the target was <90°. Only tracking periods, in which the initial Euclidean distance between the mouse

781   and cricket was >20 cm were analyzed.

782   C. The t_{end} point for the capture period was taken to be the point 6 cm away from the cricket,

783   following which a cricket captured and consumed.

784   The start points of the hunt epochs were defined as follows:

785   A. The t_{start} for the detect period was the frame 500 ms prior to the detect t_{end} point.

786   B. The t_{start} for the tracking period was the first frame after the t_{end} detect frame.

787   C. The t_{start} for the capture period was either; (1) the first period in which the mouse approached

788   the cricket and directly caught it, or (2) the first frame in which the mouse approached the cricket and all

789   subsequent cricket escapes (prior to the final cricket capture) were less than 5cm outside the contact zone

790   (11 cm inter-animal Euclidean distance).

791   Cases in which the eye cameras were dislodged by the animal during the chase (n=4 hunt sequences) were

792   included in the dataset up until the point where the cameras were dislodged.

793

794   *Target bearing*

795   Target bearing was defined as the angle between the cricket position and the mouse's forward head

796   direction in the horizontal plane.

797

798   *Digital reconstruction of arena*

799   For the digital reconstruction, the company 3dScanlab (Cologne, Germany) was engaged to create a

800   complete scan, photo series and 3D mesh model of the arena and room, which they performed using an

801   RTC 360 3D laser scanner (Leica, Germany). The 3D point cloud produced by the laser scanner was

802   converted to a 3D mesh model, to which textures of the experiment arena obtained from photographs

803   (Nikon D810, 36 mpx) were baked.

804   The camera tracking coordinate system, in which the mouse and cricket positions were tracked, and the

805   scanned coordinate system of the 3D mesh model were aligned based on 16 fiducial points which could

806   be clearly identified in both tracking camera images and the scan. Crickets were modelled as 2cm

807   diameter, 1 cm thick disks centered on their tracked position with the disk's axis oriented parallel to

808   gravity.

809

810   *Generation of animal's eye view*

811   Each eye was modelled as a hemisphere with a 180° field of view whose equator was perpendicular to the

812   animal's gaze vector. For the projection of the environment onto the cornea, frame-wise animal's eye

813   views for both eyes were created with custom written software in C++ (g++ 7.5.0, QMake 3.1, Qt 5.9.5,

814   libopenexr 2.2.0, libpng 1.6.34 and OpenGL-core-profile 4.6.0) on a GeForce RTX 2070 (NVidia driver

815   450.66), using first cube mapping followed by a transformation into a spherical coordinate system. To do

816   this, individual frame-wise coordinate transformations were made using the eye locations and

817   orientations determined as described above to transform the mesh model of the arena and cricket to a

818   static eye coordinate system using custom written vertex shaders to perform the coordinate

819   transformation and the fragment shaders to texture the mesh. A cube-map (1024 x 1024 pixels per face)

820   was created by performing such coordinate transformations for a 90 degree view in the direction of the

821   optical axis of the eye and four mutually orthogonal directions. Custom written code was then used to

822   transform the cube-map into a spherical coordinate system, with a 180 degree opening angle, using vertex

823   shaders, resulting in a 1024 x 1024 pixel frame exported as png and OpenEXR files. In addition to the color

824   map, maps of depth (pixel-wise object intersection distance), object identification and 3D position of the

825   object intersection point in the contralateral eye's coordinate system were also generated.

826

827   *Prey image probability density maps*

828   For generation of the prey image probability density maps, animal's eye views were rendered that

829   contained the cricket only (i.e. without inclusion of arena and room). Density maps from multiple detect-

830   track sequences, and multiple animals, were made by averaging.

831

832   *Ocular Alignment*

833   Ocular alignment was defined as the consistency of the projection of a given point in the eye view of one

834   eye into the other in an infinitely distant environment. This is equivalent to a projection in an idealized

835   finite-distant spherical environment while assuming a distance between the animal's eyes of 0. For

836   calculation, the radius of the sphere can then be set to 1 (without loss of generality). A point, located at

837   the center of mass of the functional focus in each eye, was chosen from which to calculate the degree of

838   inter-ocular alignment. This point was projected from one eye to the sphere surface and into the

839   contralateral eye. The degree of alignment between the two eyes was calculated as follows:

840   Let

841    $$R_i, L_i \colon \mathbb{R}^3 \to \mathbb{R}^3$$

842   be the affine transformations for the left and right eye, and let

843

844    $$E \subseteq \mathbb{R}^3$$

845   be the idealized environment. For a given direction $u \in S^2$ we calculate the projection into the right eye

846    $p_i \in \mathbb{R}^3$ by:

847    $$p_i = L_i^{-1} \cdot R_i \cdot u$$

848   The average alignment is then calculated using the formula:

849
$$\overline{\sum} 2 \cdot arcsin\big(|p_i - \langle \overline{\sum} p_i \rangle|/2\big)$$

850   where $\overline{\sum} p_i$ denotes mean and $\langle \ \ \rangle$ denotes normalization.

851

852   *Visual field overlap*

853   Visual field overlap was analyzed in the idealized finite-distant spherical environment described above for

854   ocular alignment. Visual overlap was calculated from the frame-wise maps of 3D object intersection points

855   in the contralateral eye (see above section "*Generation of animal's eye view*") generated for the ocular

856   alignment analysis: pixels whose 3D object intersection points had an angle of less than 90° to the optical

857   axis were considered part of the overlapping field of view. Probability maps of overlap were calculated by

858   averaging.

859   For analyses of the effect of freezing eye movements, eye rotations (horizontal, vertical and torsional)

860   were set to the mean rotation in one eye, and the effect quantified in the other eye view.

861

862   *Optic flow*

863   To calculate the optic flow in a given pixel for a given eye, we consider the difference vector between the

864   3D positions in the static eye coordinate system of the object intersection point for this pixel one frame

865   before and after the frame of interest, divided by $2 \cdot dt$ and mapped to unit distance by dividing by the

866   distance between eye and interception point. This yields a 3D motion vector which is independent of

867   influences of the frame rate. The spherical projection used in the rendering process described above is a

868   non-conformal, locally non-isometric map, meaning that angles between lines and distances between

869   points are not preserved. This makes it necessary to evaluate the flow in each point in a local, orthonormal

870   3D coordinate system defined by the direction vector between the eye position and the object

871   intersection point and derivative vectors along the angular coordinates $v\theta$ and $v\varphi$ at that point. Thus, we

872   define the 2D flow at a given point as the orthogonal projection of the 3D flow vector onto the local plane

873   spanned by $v\theta$ and $v\varphi$. In this study, we only use the first two components of the vector, while the third

874   component contains the motion in radial direction to the eye.

875   In Figure 5C optic flow was calculated for the animal in the idealized spherical environment described

876   above, meaning the animal's head was equidistant to the surrounding at all points. This simplified scene

877   was characterized as follows. Let

878
$$h \in \mathbb{R}^3$$

879   be the coordinate of the center of the mouse's head, then the scene around it was defined as

880
$$\{p \in \mathbb{R}^3 \mid p_z = 0 \ \cup |p - h| = r\}$$

881

882   with r = 50 cm. For optic flow calculations the sphere is considered fixed in global coordinates, and the

883   flow is evaluated at the point where the mouse is in the center of the sphere translating forward at a

884   speed of 1 cm/s.

885   In Figure 5E optic flow was calculated with the animal in the digitally reconstructed environment (see

886   above).

887

888   *Coloring of optic flow poles in mouse corneal views*

889   The points in the scatter plot of optic flow poles in mouse corneal views were color-coded for the

890   density of neighboring points using a two-dimensional Gaussian smoother with standard deviation

891
$$\sigma = \frac{2\pi}{180}$$

892   For a given point, the density was calculated as:

893
$$s_i = \sum_{j \in F} \frac{1}{2\pi\sigma^2} \exp\left(\frac{-|x_i - x_j|^2}{2 \cdot \sigma^2}\right)/|F|$$

894   where F is the set of all considered frame indices, and

895
$$x_i = \frac{\partial_h[p]_i}{|\partial_h[p]_i|}$$

896   where $\partial_h[p]_i$ is the discrete central difference quotient of the mouse's eye trajectory *p* in frame *i,* in the

897   coordinate system of the respective eye, evaluated over h=4 frames.

898

899   *Mouse Eye Model*

900   When constructing the eye model, we took experimentally determined values from (Barathi, Boopathi et

901   al. 2008) (see Table 1). While we recognize that this study employed a different strain of mice to the one

902   used here, the methodology used provides estimates of physical and optical parameters measured under

903   conditions closest to those relevant for the current study. Further, variation of these parameters was not

904   found to change the model to an extent that would influence the conclusions drawn from analyses

905   involving the eye model (see below). These values distinctly define the spatial shapes and positions of the

906   refractive components of the model eye (Figure 3A), as well as refractive indices for all but the lens, n_{lens}.

907   We further assume a pupil radius of 594 μm, which is the mean of constricted and dilated mouse pupil

908   sizes from (Pennesi, Lyubarsky et al. 1998). We define the focal point of a bundle of rays as the point with

909   minimal least squares distance to the rays. To optimize the missing refractive index $n_{lens} : \Omega \rightarrow R^+$

910   inside the lens body $\Omega \subset \mathbb{R}^3$, we first calculated two lens models and optimized them such that the focal

911   point of 10000 rays emitted from an object at 10 cm distance on the optical axis lay on the retina. The

912   first model, for optimization of the lens surface, was derived with optimal constant refractive index $n_c \in$

913   R^+over the volume. The second model, for lens gradient optimization, was derived with a smooth

914   transition of refractive index to the anterior and posterior lens boundary, ie. $n_b = 1.333$ on $\partial\Omega$. We then

915   used Poisson's equation $\Delta\, n_g = c$, and optimized the strength of the gradient $c \,\in\, R^+$. We assumed the

916   final lens model as a linear combination of these two models:

917    $$n_{lens} = \alpha \cdot n_c + (1 - \alpha) \cdot n_g$$

918   with $\alpha \,\in\, [0,1]$, where we optimized α as described for the above models, but from a point 10 cm away

919   and 45° off optical axis. The derived refractive indices (Table 2) were within the range measured in (Cheng,

920   Parreno et al. 2019).

921   To test the sensitivity of the model to changes in assumed physical parameters, we systematically changed

922   the radius of curvatures listed in Table 1, and the thickness listed in Table 2 by 10, 50 and 100 µm (several

923   different values were used, to check the linearity of the dependence). We calculated the propagation of

924   uncertainty through the eye model by analyzing the variation of radial elevation on the retina of the 45

925   rays (above), taking the numerical differentiation of each input variable that was used in the model. Lens

926   optimization was performed for each newly generated eye model (as described above). The maximum

927   deviations were 0.4, 1.38, 2.76 degrees respectively for the 10, 50 and 100 µm changes (Figure 7E), and

928   overall none of the observed effects on the model would influence the conclusions drawn from the

929   analyses performed using the eye model.

930

931

932   *Projection from retina to cornea*

933   The refractive elements in the rodent eye do not behave like ideally corrected optical elements, with the

934   result that there is a distribution of incident rays with slightly varying angles of incidence on the cornea

935   which converge on any given point on the retina. Projection from retina to cornea therefore requires an

936   estimate of the distribution of outside world angles of incidence for any point of interest on the retina. To

937   do this, we used a Monte-Carlo simulation to back-trace through the optics a set of randomly chosen rays

938   emerging from the point of interest on the retina. Since the intensity of light on a surface with an incoming

939   angle of θ is proportional to $\cos(\theta)$, this function was also chosen for the probability density distribution

940   of ray exit angles. The rays were then traced until they either hit any opaque surface, resulting in the

941   affected ray being discarded, or passed through the anterior cornea, in which case the ray was accepted

942   and its angle added to the distribution of passing exit angles for the respective point on the retina.

943   Refraction on boundary layers between different indices of refraction was performed analytically

944   according to Snell's law. In volumes with a continuous variable refractive index (i.e. gradient-index (GRIN)

945   optics), we used a finite-elements model. We first discretized the lens as a 40x40x40 lattice of side length

946   2.4 mm. We then started from initial conditions where s(0) is the point of incidence and v(0) is the vector

947   of incidence multiplied by the speed of light c. The subsequent discrete trajectory and direction of

948   propagation is then calculated step-wise according to

949
$$s(t_{i+1}) := s(t_i) + v(t_i) \cdot (t_{i+1} - t_i)$$

950

951
$$\tilde{v}(t_{i+1}) := \tilde{v}(t_i) + \nabla \log n\big(s(t_{i+1})\big) \cdot (t_{i+1} - t_i)$$

952

953
$$v(t_i) := \frac{\tilde{v}(t_i)}{|\tilde{v}(t_i)|^2}$$

954   The gradient is calculated in the lens lattice as the three-dimensional difference quotient, and then

955   linearly interpolated to the exact position $s(t_i)$ of the ray.

956

957   *Projection of retinal ganglion cell density contours onto the model eye cornea*

958   To determine the corneal location corresponding to the histologically identified retinal specialization in

959   the mouse, isodensity lines were redrawn from (Drager and Olsen 1980) in Illustrator and digitized using

960   Matlab. Isodensity lines enclosing regions containing the highest and second highest density of retinal

961   ganglion cells, as well as the optic disc and outline of the retinal whole mount, were redrawn directly from

962   Figure 3A in (Drager and Olsen 1981), with horizontal being taken as horizontal (nasal-temporal) in the

963   figure. The isodensity lines were scaled to match the eye diameter used for model eye, then placed into

964   the model eye such that the center of mass of the optic disc reconstructed with the retinal ganglion cell

965   contours was coincident with the intersection of the optic axis and retina in the eye model (Supplementary

966   Figure 2A-C). As the eye model was rotationally symmetrical, no further alignment between the histology

967   and eye model was necessary. The high retinal ganglion cell density regions were then back-projected

968   from retina to cornea as described above (Supplementary Figure 2D-E).

969

970   *Eye in head coordinates*

971   To quantify the effect of head rotations on VOR evoked eye movements in a common coordinate system,

972   head rotations were normalized such that the average pitch and roll were 0. Axes were labeled X and Y

973   respectively and eye rotations were represented using this horizon-aligned X-Y coordinate system.

974   Positive head X values indicate head pitched up, while negative head X values indicate head pitched down.

975   Negative head Y values indicate roll left, while positive Y values indicate roll right. Comparisons of the

976   relationship between head and eye rotations were carried out using differential rotations between frame

977   and average pose, defined in the following way:

978     $l': L \rightarrow G, r': R \rightarrow G, h: H \rightarrow G$ are the affine transformations between Cartesian global coordinate system

979   G, head-fixed coordinate system H and left/right-eye coordiante systems L/R.

980

981   The transformations from L/R respectively to H are:

982
$$l = h^{-1} \cdot l'$$

983
$$r = h^{-1} \cdot r'$$

984   We calculate the left and right eye differential rotations as:

985
$$l_{delta} = l \cdot \bar{l}^{-1}$$

986
$$r_{delta} = r \cdot \bar{r}^{-1}$$

987   where $\bar{l}$ and $\bar{r}$ denote the average transformations over all frames (chordal L2 mean, implementation

988   from SciPy 1.4.1).

989

990   *Statistical Analysis*

991   Within one experimental trial, the experimentally measured variables of interest are highly correlated

992   with each other. This fact prevents us from using standard statistical tests on the whole time-trace to

993   establish if any difference we observed in the data across different experimental conditions are significant

994   or not, as one requirement of these kind on tests is that the samples from the populations being compared

995   are independent of each other. However, we realized that trial-to-trial variability is the dominant source

996   of variability in the data, whereas within-trial variability explains a smaller fraction of the total variance

997   observed (a more detailed report is found in Table 4). For this reason, we decided to represent each

998   temporal trace by its median value. We used the median and not the mean, because the former is more

999   resistant to the presence of outliers and it is better suited to represent the "average" value of a variable

1000   in this context. This operation reduced the size of the dataset to one data points per trial, which we can

1001   reasonably assume to be independent of each other.

1002

1003   **Movie 1.** Digitized and rendered view of the experiment arena and surrounding environment. Laser
1004   scanned and digitally reconstructed experiment environment, providing distance and positional
1005   information of objects within the mouse's environment. When combined with the tracked 3D cricket
1006   positions and the tracked mouse head and eye positions and rotations this allowed the generation of a
1007   frame-by-frame mouse eye view of the prey and the surroundings.
1008

1009   **Movie 2.** Mouse eye views during cricket detection and tracking. Upper panels: Digitally rendered mouse

1010   left and right eye view's of its prey (cricket - red) and the surrounding environment during prey detection,

1011   tracking and prey escape. Lower panel: recorded pursuit sequence. Green points indicate the tracked

1012   cricket body center. Note the transition from a peripheral monocular to a binocular lower nasal location

1013   within the visual fields. Note also the large overhead visual field.

1014

References:

1016 Angelaki, D. E. and B. J. Hess (2005). "Self-motion-induced eye movements: effects on visual acuity and
1017 navigation." <u>Nat Rev Neurosci</u> **6**(12): 966-976.
1018 Badan, D. (1986). "Diet of the House Mouse (Mus-Musculus L) in 2 Pine and a Kauri Forest." <u>New Zealand</u>
1019 <u>Journal of Ecology</u> **9**: 137-141.
1020 Baden, T., P. Berens, K. Franke, M. Roman Roson, M. Bethge and T. Euler (2016). "The functional diversity
1021 of retinal ganglion cells in the mouse." <u>Nature</u> **529**(7586): 345-350.
1022 Barathi, V. A., V. G. Boopathi, E. P. Yap and R. W. Beuerman (2008). "Two models of experimental myopia
1023 in the mouse." <u>Vision Res</u> **48**(7): 904-916.
1024 Bleckert, A., G. W. Schwartz, M. H. Turner, F. Rieke and R. O. Wong (2014). "Visual space is represented
1025 by nonmatching topographies of distinct mouse retinal ganglion cell types." <u>Curr Biol</u> **24**(3): 310-315.
1026 Boursot, P., J. C. Auffray, J. Brittondavidian and F. Bonhomme (1993). "The Evolution of House Mice."
1027 <u>Annual Review of Ecology and Systematics</u> **24**: 119-152.
1028 Chakraborty, R., K. D. Lacy, C. C. Tan, H. N. Park and M. T. Pardue (2014). "Refractive index measurement
1029 of the mouse crystalline lens using optical coherence tomography." <u>Exp Eye Res</u> **125**: 62-70.
1030 Cheng, C., J. Parreno, R. B. Nowak, S. K. Biswas, K. Wang, M. Hoshino, K. Uesugi, N. Yagi, J. A. Moncaster,
1031 W. K. Lo, B. Pierscionek and V. M. Fowler (2019). "Age-related changes in eye lens biomechanics,
1032 morphology, refractive index and transparency." <u>Aging (Albany NY)</u> **11**(24): 12497-12531.
1033 Dean, P., P. Redgrave and G. W. Westby (1989). "Event or emergency? Two response systems in the
1034 mammalian superior colliculus." <u>Trends Neurosci</u> **12**(4): 137-147.
1035 Dhande, O. S., B. K. Stafford, J. A. Lim and A. D. Huberman (2015). "Contributions of Retinal Ganglion Cells
1036 to Subcortical Visual Processing and Behaviors." <u>Annu Rev Vis Sci</u> **1**: 291-328.
1037 Drager, U. C. (1978). "Observations on monocular deprivation in mice." <u>J Neurophysiol</u> **41**(1): 28-42.
1038 Drager, U. C. and J. F. Olsen (1980). "Origins of crossed and uncrossed retinal projections in pigmented
1039 and albino mice." <u>J Comp Neurol</u> **191**(3): 383-412.
1040 Drager, U. C. and J. F. Olsen (1981). "Ganglion cell distribution in the retina of the mouse." <u>Invest</u>
1041 <u>Ophthalmol Vis Sci</u> **20**(3): 285-293.
1042 Franke, K., P. Berens, T. Schubert, M. Bethge, T. Euler and T. Baden (2017). "Inhibition decorrelates visual
1043 feature representations in the inner retina." <u>Nature</u> **542**(7642): 439-444.
1044 Garrett, M. E., I. Nauhaus, J. H. Marshel and E. M. Callaway (2014). "Topography and areal organization of
1045 mouse visual cortex." <u>J Neurosci</u> **34**(37): 12587-12600.
1046 Gibson, J. J., P. Olum and F. Rosenblatt (1955). "Parallax and perspective during aircraft landings." <u>Am J</u>
1047 <u>Psychol</u> **68**(3): 372-385.
1048 Gire, D. H., V. Kapoor, A. Arrighi-Allisan, A. Seminara and V. N. Murthy (2016). "Mice Develop Efficient
1049 Strategies for Foraging and Navigation Using Complex Natural Stimuli." <u>Curr Biol</u> **26**(10): 1261-1273.
1050 Hoy, J. L., H. I. Bishop and C. M. Niell (2019). "Defined Cell Types in Superior Colliculus Make Distinct
1051 Contributions to Prey Capture Behavior in the Mouse." <u>Curr Biol</u> **29**(23): 4130-4138 e4135.
1052 Hoy, J. L., I. Yavorska, M. Wehr and C. M. Niell (2016). "Vision Drives Accurate Approach Behavior during
1053 Prey Capture in Laboratory Mice." <u>Curr Biol</u> **26**(22): 3046-3052.
1054 Huberman, A. D., M. Manu, S. M. Koch, M. W. Susman, A. B. Lutz, E. M. Ullian, S. A. Baccus and B. A. Barres
1055 (2008). "Architecture and activity-mediated refinement of axonal projections from a mosaic of genetically
1056 identified retinal ganglion cells." <u>Neuron</u> **59**(3): 425-438.
1057 Hughes, A. (1977). The topography of vision in mammals of contrasting life style: comparative optics and
1058 retinal organization. <u>Handbook of Sensory Physiology VII</u>. F. Crescitelli. Berlin, Springer-Verlag. **VII**.
1059 Hughes, A. (1979). "A schematic eye for the rat." <u>Vision Res</u> **19**(5): 569-588.

Ibrahim, L. and E. A. Wright (1975). "The growth of rats and mice vibrissae under normal and some abnormal conditions." J Embryol Exp Morphol **33**(4): 831-844.

Jeon, C. J., E. Strettoi and R. H. Masland (1998). "The major cell populations of the mouse retina." J Neurosci **18**(21): 8936-8946.

Johnson, G. L. and H. F. Gadow (1901). "I. Contributions to the comparative anatomy of the mammalian eye, chiefly based on ophthalmoscopic examination." Philosophical Transactions of the Royal Society of London. Series B, Containing Papers of a Biological Character **194**(194-206): 1-82.

Johnson, K. P., M. J. Fitzpatrick, L. Zhao, B. Wang, S. McCracken, P. R. Williams and D. Kerschensteiner (2021). "Cell-type-specific binocular vision guides predation in mice." Neuron.

Krieger, B., M. Qiao, D. L. Rousso, J. R. Sanes and M. Meister (2017). "Four alpha ganglion cell types in mouse retina: Function, structure, and molecular signatures." PLoS One **12**(7): e0180091.

La Chioma, A., T. Bonhoeffer and M. Hubener (2019). "Area-Specific Mapping of Binocular Disparity across Mouse Visual Cortex." Curr Biol **29**(17): 2954-2960 e2955.

La Chioma, A., T. Bonhoeffer and M. Hubener (2020). "Disparity Sensitivity and Binocular Integration in Mouse Visual Cortex Areas." J Neurosci **40**(46): 8883-8899.

Laing, R. J., J. Turecek, T. Takahata and J. F. Olavarria (2015). "Identification of Eye-Specific Domains and Their Relation to Callosal Connections in Primary Visual Cortex of Long Evans Rats." Cerebral Cortex **25**(10): 3314-3329.

Land, M. F. (1999). "Motion and vision: why animals move their eyes." J Comp Physiol A **185**(4): 341-352.

Langley, W. M. (1983). "Relative Importance of the Distance Senses in Grasshopper Mouse Predatory Behavior." Animal Behaviour **31**(Feb): 199-205.

Langley, W. M. (1984). "Recognition of prey species by their odors in the grasshopper mouse (Onychomys leucogaster)." Behav Processes **9**(2-3): 277-280.

Langley, W. M. (1988). "Spiny mouse's (Acomys Cahirinus) use of its distance senses in prey localization." Behav Processes **16**(1-2): 67-73.

Lappe, M., F. Bremmer and A. V. van den Berg (1999). "Perception of self-motion from visual flow." Trends in Cognitive Sciences **3**(9): 329-336.

Lettvin, J. Y., H. R. Maturana, W. S. Mcculloch and W. H. Pitts (1959). "What the Frogs Eye Tells the Frogs Brain." Proceedings of the Institute of Radio Engineers **47**(11): 1940-1951.

Martersteck, E. M., K. E. Hirokawa, M. Evarts, A. Bernard, X. Duan, Y. Li, L. Ng, S. W. Oh, B. Ouellette, J. J. Royall, M. Stoecklin, Q. Wang, H. Zeng, J. R. Sanes and J. A. Harris (2017). "Diverse Central Projection Patterns of Retinal Ganglion Cells." Cell Rep **18**(8): 2058-2072.

Meyer, A. F., J. O'Keefe and J. Poort (2020). "Two Distinct Types of Eye-Head Coupling in Freely Moving Mice." Curr Biol **30**(11): 2116-2130.e2116.

Meyer, A. F., J. Poort, J. O'Keefe, M. Sahani and J. F. Linden (2018). "A Head-Mounted Camera System Integrates Detailed Behavioral Monitoring with Multichannel Electrophysiology in Freely Moving Mice." Neuron **100**(1): 46-60 e47.

Michaiel, A. M., E. T. Abe and C. M. Niell (2020). "Dynamics of gaze control during prey capture in freely moving mice." Elife **9**.

Murphy, G. J. and F. Rieke (2006). "Network variability limits stimulus-evoked spike timing precision in retinal ganglion cells." Neuron **52**(3): 511-524.

Niell, C. M. and M. P. Stryker (2008). "Highly selective receptive fields in mouse visual cortex." J Neurosci **28**(30): 7520-7536.

Olavarria, J. and R. C. van Sluyters (1983). "Widespread callosal connections in infragranular visual cortex of the rat." Brain Research **279**: 233-237.

Oommen, B. S. and J. S. Stahl (2008). "Eye orientation during static tilts and its relationship to spontaneous head pitch in the laboratory mouse." Brain Res **1193**: 57-66.

1107   Pang, J. J., F. Gao and S. M. Wu (2003). "Light-evoked excitatory and inhibitory synaptic inputs to ON and
1108   OFF alpha ganglion cells in the mouse retina." J Neurosci **23**(14): 6063-6073.
1109   Payne, H. L. and J. L. Raymond (2017). "Magnetic eye tracking in mice." Elife **6**.
1110   Pennesi, M. E., A. L. Lyubarsky and E. N. Pugh, Jr. (1998). "Extreme responsiveness of the pupil of the dark-
1111   adapted mouse to steady retinal illumination." Invest Ophthalmol Vis Sci **39**(11): 2148-2156.
1112   Philipson, B. (1969). "Distribution of protein within the normal rat lens." Invest Ophthalmol **8**(3): 258-270.
1113   Procacci, N. M., K. M. Allen, G. E. Robb, R. Ijekah, H. Lynam and J. L. Hoy (2020). "Context-dependent
1114   modulation of natural approach behaviour in mice." Proc Biol Sci **287**(1934): 20201189.
1115   Ramachandra, V., V. Pawlak, D. J. Wallace and J. N. D. Kerr (2020). "Impact of visual callosal pathway is
1116   dependent upon ipsilateral thalamus." Nat Commun **11**(1): 1889.
1117   Reese, B. E. and A. Cowey (1986). "Large retinal ganglion cells in the rat: their distribution and laterality
1118   of projection." Exp Brain Res **61**(2): 375-385.
1119   Sabbah, S., J. A. Gemmer, A. Bhatia-Lin, G. Manoff, G. Castro, J. K. Siegel, N. Jeffery and D. M. Berson
1120   (2017). "A retinal code for motion along the gravitational and body axes." Nature **546**(7659): 492-497.
1121   Saleem, A. B. (2020). "Two stream hypothesis of visual processing for navigation in mouse." Curr Opin
1122   Neurobiol **64**: 70-78.
1123   Salinas-Navarro, M., M. Jimenez-Lopez, F. J. Valiente-Soriano, L. Alarcon-Martinez, M. Aviles-Trigueros, S.
1124   Mayor, T. Holmes, R. D. Lund, M. P. Villegas-Perez and M. Vidal-Sanz (2009). "Retinal ganglion cell
1125   population in adult albino and pigmented mice: a computerized analysis of the entire population and its
1126   spatial distribution." Vision Res **49**(6): 637-647.
1127   Samonds, J. M., V. Choi and N. J. Priebe (2019). "Mice Discriminate Stereoscopic Surfaces Without Fixating
1128   in Depth." J Neurosci **39**(41): 8024-8037.
1129   Scholl, B., J. Burge and N. J. Priebe (2013). "Binocular integration and disparity selectivity in mouse primary
1130   visual cortex." J Neurophysiol **109**(12): 3013-3024.
1131   Scholl, B., J. J. Pattadkal, G. A. Dilly, N. J. Priebe and B. V. Zemelman (2015). "Local Integration Accounts
1132   for Weak Selectivity of Mouse Neocortical Parvalbumin Interneurons." Neuron **87**(2): 424-436.
1133   Schuett, S., T. Bonhoeffer and M. Hubener (2002). "Mapping retinotopic structure in mouse visual cortex
1134   with optical imaging." J Neurosci **22**(15): 6549-6559.
1135   Shang, C., A. Liu, D. Li, Z. Xie, Z. Chen, M. Huang, Y. Li, Y. Wang, W. L. Shen and P. Cao (2019). "A subcortical
1136   excitatory circuit for sensory-triggered predatory hunting in mice." Nat Neurosci **22**(6): 909-920.
1137   Stabio, M. E., K. B. Sondereker, S. D. Haghgou, B. L. Day, B. Chidsey, S. Sabbah and J. M. Renna (2018). "A
1138   novel map of the mouse eye for orienting retinal topography in anatomical space." J Comp Neurol **526**(11):
1139   1749-1759.
1140   Sterratt, D. C., D. Lyngholm, D. J. Willshaw and I. D. Thompson (2013). "Standard anatomical and visual
1141   space for the mouse retina: computational reconstruction and transformation of flattened retinae with
1142   the Retistruct package." PLoS Comput Biol **9**(2): e1002921.
1143   Szatko, K. P., M. M. Korympidou, Y. Ran, P. Berens, D. Dalkara, T. Schubert, T. Euler and K. Franke (2020).
1144   "Neural circuits in the mouse retina support color vision in the upper visual field." Nat Commun **11**(1):
1145   3481.
1146   Szel, A., P. Rohlich, A. R. Caffe, B. Juliusson, G. Aguirre and T. Van Veen (1992). "Unique topographic
1147   separation of two spectral classes of cones in the mouse retina." J Comp Neurol **325**(3): 327-342.
1148   Tann, C. R., G. R. Singleton and B. J. Coman (1991). "Diet of the House Mouse, Mus-Domesticus, in the
1149   Mallee-Wheatlands of North-Western Victoria." Wildlife Research **18**(1): 1-12.
1150   van Alphen, B., B. H. Winkelman and M. A. Frens (2010). "Three-dimensional optokinetic eye movements
1151   in the C57BL/6J mouse." Invest Ophthalmol Vis Sci **51**(1): 623-630.
1152   van Wyk, M., H. Wassle and W. R. Taylor (2009). "Receptive field properties of ON- and OFF-ganglion cells
1153   in the mouse retina." Vis Neurosci **26**(3): 297-308.

1154   Wagor, E., N. J. Mangini and A. L. Pearlman (1980). "Retinotopic organization of striate and extrastriate
1155   visual cortex in the mouse." <u>J Comp Neurol</u> **193**(1): 187-202.
1156   Wallace, D. J., D. S. Greenberg, J. Sawinski, S. Rulla, G. Notaro and J. N. Kerr (2013). "Rats maintain an
1157   overhead binocular field at the expense of constant fusion." <u>Nature</u> **498**(7452): 65-69.
1158   Yilmaz, M. and M. Meister (2013). "Rapid innate defensive responses of mice to looming visual stimuli."
1159   <u>Curr Biol</u> **23**(20): 2011-2015.
1160   Zhang, Y., I. J. Kim, J. R. Sanes and M. Meister (2012). "The most numerous ganglion cell type of the mouse
1161   retina is a selective feature detector." <u>Proc Natl Acad Sci U S A</u> **109**(36): E2391-2398.
1162   Zhao, Z. D., Z. Chen, X. Xiang, M. Hu, H. Xie, X. Jia, F. Cai, Y. Cui, Z. Chen, L. Qian, J. Liu, C. Shang, Y. Yang,
1163   X. Ni, W. Sun, J. Hu, P. Cao, H. Li and W. L. Shen (2019). "Zona incerta GABAergic neurons integrate prey-
1164   related sensory signals and induce an appetitive drive to promote hunting." <u>Nat Neurosci</u> **22**(6): 921-932.

1165

1166

1167 **Author contributions:**

1168 **1. Carl D. Holmgren**

1169 Department of Behavior and Brain Organization, Research Center Caesar, Bonn, Germany

1170 Contribution: Conceptualization; Methodology; Validation; Formal analysis; Investigation; Data curation;
1171 Writing – original draft preparation; Writing – review & editing; Visualization

1172 Competing Interests: No competing interests declared

1173 **2. Paul Stahr**

1174 Department of Behavior and Brain Organization, Research Center Caesar, Bonn, Germany

1175 Contribution: Methodology; Software; Validation; Formal analysis; Investigation; Data curation; Writing –

1176 review & editing; Visualization.

1177 Competing Interests: No competing interests declared

1178 **3. Damian J. Wallace**

1179 Department of Behavior and Brain Organization, Research Center Caesar, Bonn, Germany

1180 Contribution: Conceptualization; Methodology; Formal analysis; Data curation; Writing – original draft

1181 preparation; Writing – review & editing; Visualization; Supervision.

1182 Competing Interests: No competing interests declared

1183 **4. Kay-Michael Voit**

1184 Department of Behavior and Brain Organization, Research Center Caesar, Bonn, Germany

1185 Contribution: Methodology; Software; Validation; Formal analysis; Resources; Data curation; Writing –
1186 review & editing; Supervision.

1187 Competing Interests: No competing interests declared

1188 **5. Emily J. Matheson**

1189 Department of Behavior and Brain Organization, Research Center Caesar, Bonn, Germany

1190 Contribution: Methodology; Resources

1191 Competing Interests: No competing interests declared

1192 **6. Juergen Sawinski**

1193 Department of Behavior and Brain Organization, Research Center Caesar, Bonn, Germany

1194 Contribution: Methodology; Resources.

1195 Competing Interests: No competing interests declared

1196 **7. Giacomo Bassetto**

1197 Department of Behavior and Brain Organization, Research Center Caesar, Bonn, Germany

1198 Contribution: Formal analysis.

1199 Competing Interests: No competing interests declared

1200 **8. Jason N. D. Kerr**

1201 Department of Behavior and Brain Organization, Research Center Caesar, Bonn, Germany

1202 Contribution: Conceptualization; Methodology; Formal analysis; Data curation; Writing – original draft
1203 preparation; Writing – review & editing; Visualization; Supervision; Funding acquisition.

1204 Competing Interests: No competing interests declared

1205

1206
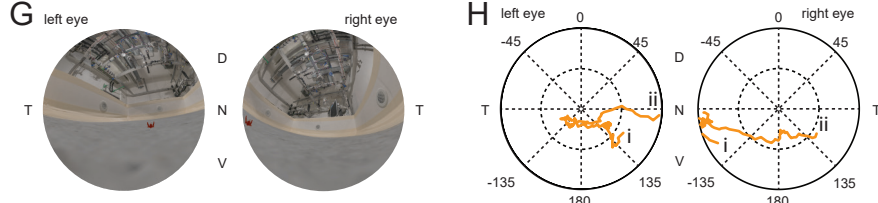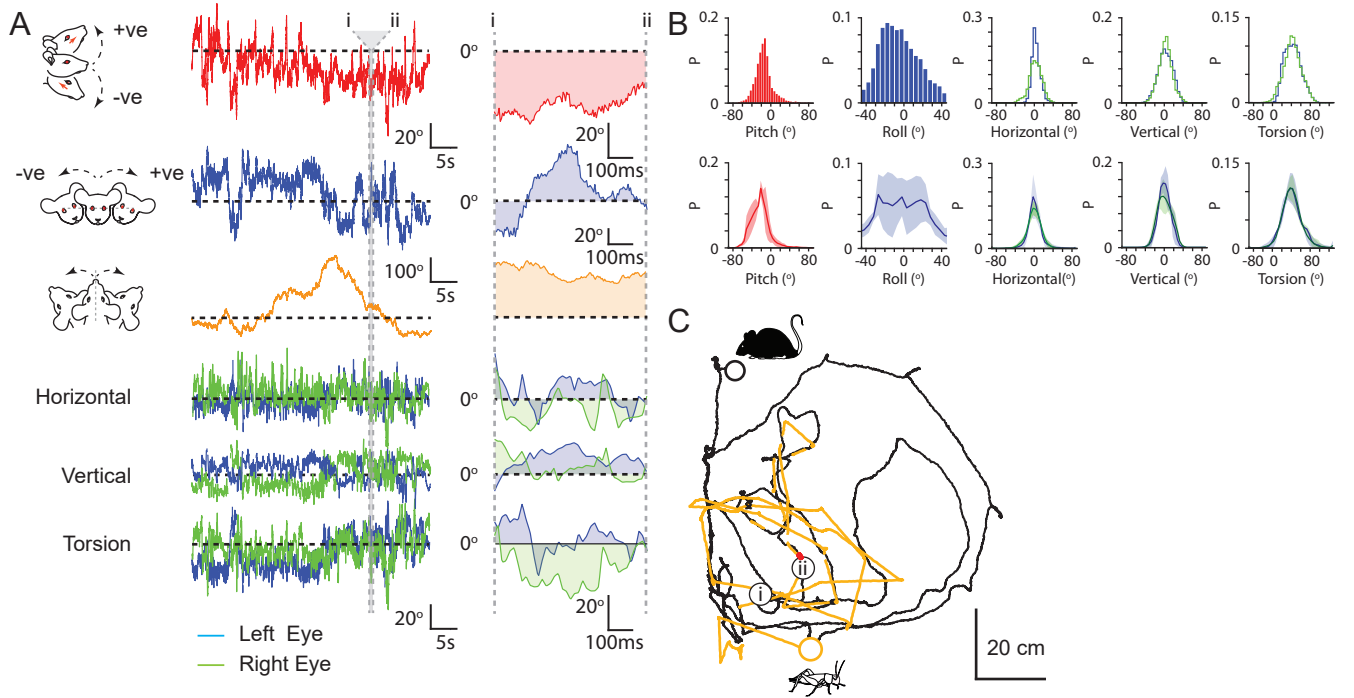
Figure 1 – figure supplement 1

Generation of mouse eye views during cricket pursuit.

(A) Head pitch (red), roll (blue) and yaw (orange) and associated left (blue) and right (green) horizontal, vertical and torsional eye movements during the 46.2s, example cricket pursuit sequence shown in C. (Right) Head and eye rotations during the 0.65s region between i and ii in the cricket pursuit sequence in C. **(B)** Example (upper rows) head pitch (547118 frames), roll (547118 frames), and horizontal (612161 frames), vertical (547118 frames) and torsional (612161 frames), eye rotations (n=1 animal). Lower rows: head and eye rotations from 3 mice. Data for B (lower), from 1436204 frames, from 3 animals. **(C)** Mouse (black) and cricket (orange) paths during a 46.2s segment of a single pursuit sequence for one animal. **(D)** Photograph of experiment arena and surrounding environment. **(E)** Digital rendering of the same experiment arena and surrounding environment. **(F)** Top-down view of the mouse's left and right monocular and binocular fields of view (mouse's head would be centered at the intersection point of monocular and binocular fields of view). **(G)** Cricket (red) position in the rendered left and right eye corneal fields of view of the experiment arena and surrounding environment during the pursuit sequence in C. **(H)** Trajectory of the projected cricket position in the left and right corneal views, during the pursuit sequence in C.
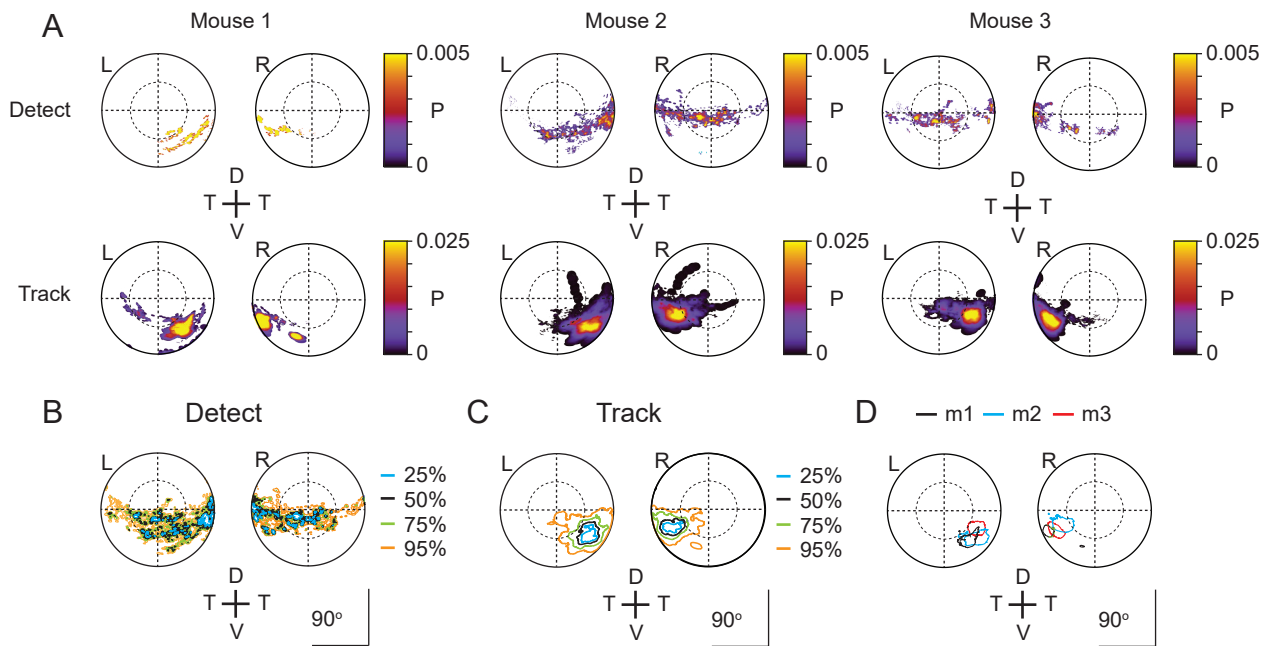
Figure 2 – figure supplement 1.
Individual corneal prey image heatmaps.
(A) Probability density maps for detect (upper row) and track (lower row) epochs for each of the three animals individually. Data from 4 detect and 5 track sequences, 27 detect and 28 track sequences and 17 detect and 19 track sequences for mouse 1, 2 and 3 respectively. (B) Isodensity contours calculated from the average probability density maps for all detect epochs from all 3 animals. (C) Isodensity contours for all track epochs from all 3 animals. (D) 50% isodensity contour (defined as in Figure 2H) during track epochs for each of the three mice (m1-m3) individually.
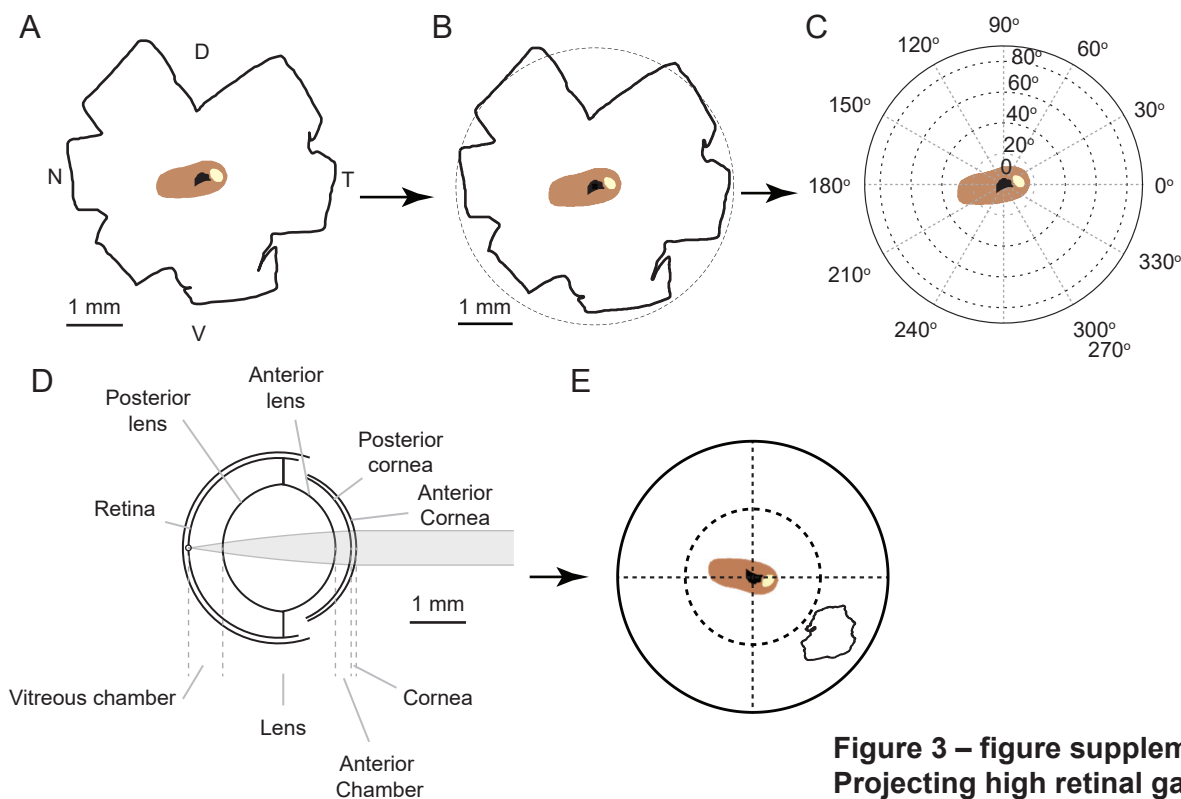
Figure 3 – figure supplement 1
Projecting high retinal ganglion cell density region from retina to cornea.
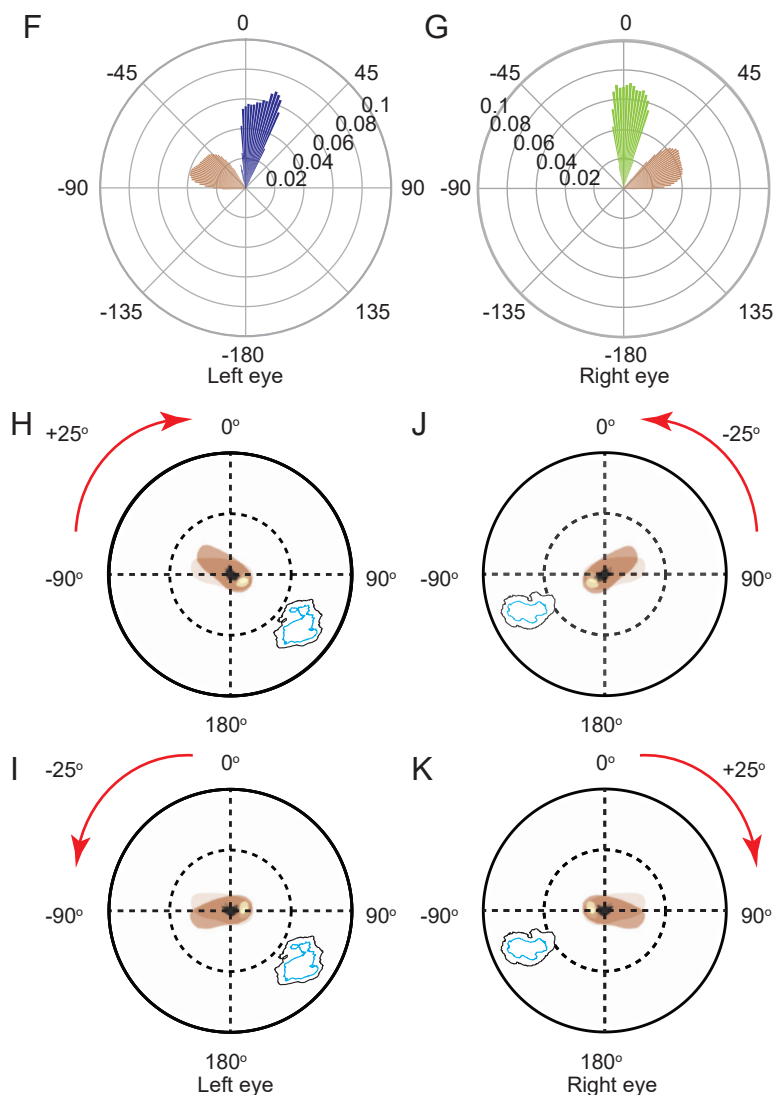
(A) Retinal whole mount redrawn from (Drager and Olsen 1981) including whole mount outline (black), and outlines of the optic disc (black) and highest (>8000 cells/mm2,beige) and second highest (>7000 cells/mm2brown) retinal ganglion cell density isodensity lines. (B) Overlay of the redrawn retinal whole mount from A and a representation of the mouse eye equatorial diameter (dashed) from (Tkachenko 2010). The center of the equatorial diameter was overlaid with the center of mass of the outline of the optic disc of the redrawn whole mount (black cross). Color coding as in A. (C) Retinal isodensity lines represented in spherical coordinates. Color coding as in A. (D) Schematic of mouse eye model (from Figure 3A). (E) Regions within the isodensity contours from A and the 50% isodensity contour from the track epochs from Figure 2H projected through the mouse eye model into the corneal view from the left eye (from Figure 3B). (F) Top-down view of the coverage region for the left eye of the 50% isodensity contour (blue) and second highest RGC region (brown). Bars represent the probability density function for the respective regions at that azimuth angle. Mouse's forward direction directed to 0o, and mouse's right directed to 90 o. (G) Top-down view of the coverage region for the right eye of the 50% isodensity contour (green) and second highest RGC region (brown). Conventions as in F. (H & I) left and (J & K) right eye corneal views, showing the effect on the orientation and location of RGC regions and isodensity contours of ± 25o torsional offsets. Original position of RGC region, beige, position after offset brown; color-coding of isodensity contours as in Figure 2H.

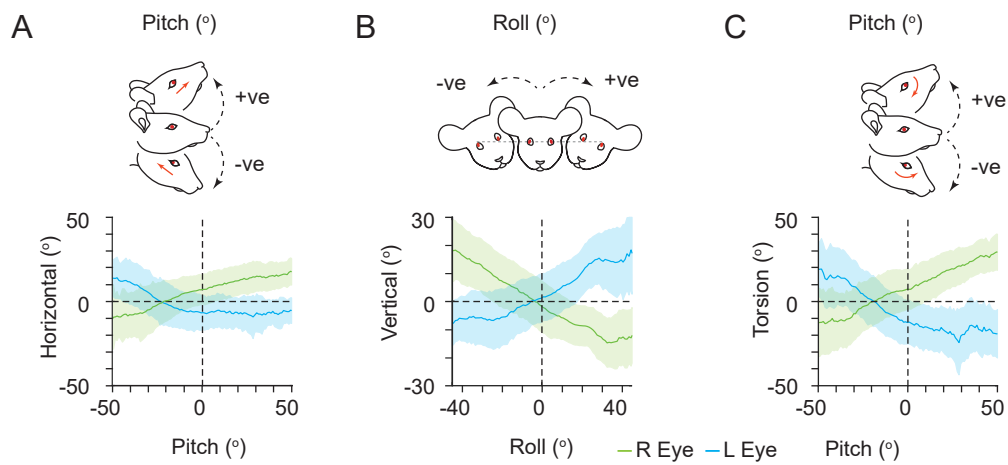**Figure 4 – figure supplement 1**
VOR relationships between head and eye rotations and alignment of left and right eyes.
(A) Relationship between mouse head pitch and horizontal eye rotations (left eye, blue; right eye, green; mean±SD). **(B)** Relationship between head roll and vertical eye rotations. Plot conventions as in A. **(C)** Relationship between head pitch and torsional eye rotations. Plot conventions as in A. Data for A-C, from 1436204 frames, from 3 animals.
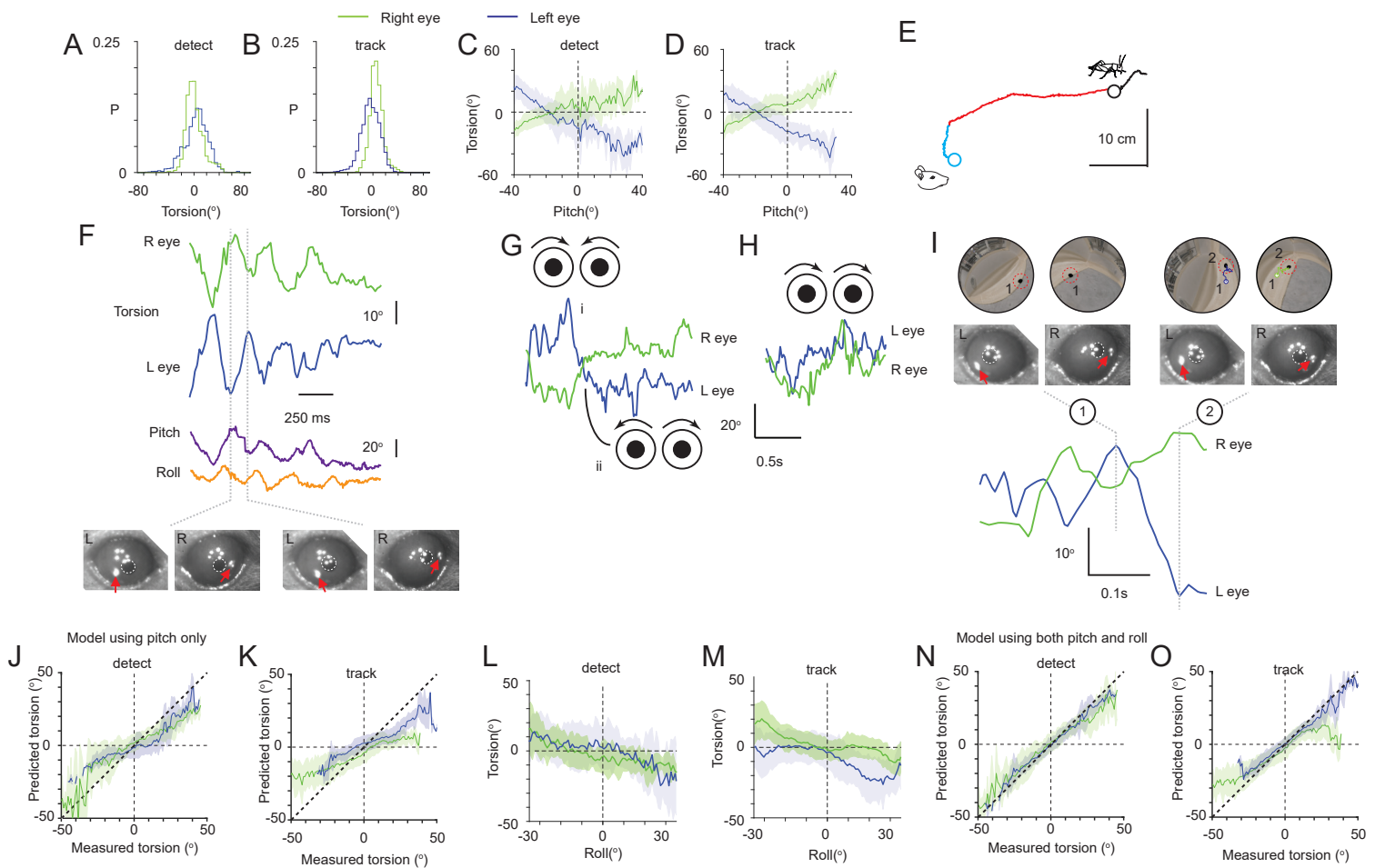
Figure 4 – figure supplement 2
Ocular torsion during cricket pursuit.
(A) Distribution of left (blue) and right (green) eye torsional rotations during detect epochs. Data from 57 epochs (4406 frames) from 3 animals. (B) Distribution of ocular torsion during track epochs. Conventions as in A. Data from 65 epochs (13624 frames) from 3 animals. (C) Average relationship (mean±SD) between head pitch and torsional eye rotations during detect epochs for left (blue and right (green) eyes. Data from 57 epochs (4406 frames) from 3 animals. (D) Average head pitch and torsional eye rotations relationships during track epochs. Conventions as in C. Data from 65 epochs (13624 frames) from 3 animals. (E) Mouse (detect epoch, blue; track epoch, red) and cricket (black) trajectories during one example pursuit sequence. (F) Torsional rotations of the left (blue) and right (green) eyes, and head pitch (purple) and roll (orange), during the pursuit sequence in E. Lower panels show example eye images from the indicated time points in the kinetic traces. Red arrows indicate tracked TiO2 spots. (G) Example sequences showing torsional rotation kinetic traces for left (blue) and right (green) eyes during in- (i) and excyclovergence (ii) from one pursuit sequence. Schematics show the ocular rotations in the left and right eyes. (H) Example sequence showing dextrocycloversion in one pursuit sequence. Conventions as in G. (I) Example of the effect of torsional rotations on prey image location. Corneal eye views of the cricket (black ellipse in red dashed circle) and arena (upper) and associated eye images (middle) at the time points indicated in the torsion kinetic traces (lower) for the left (blue) and right (green) eyes. Note cricket trajectories in left and right corneal eye views, which show the trajectory of the cricket in the corneal views between time points 1 and 2. Red arrows in eye images show TiO2 torsion tracking spots. (J) Performance of a model predicting torsion based on head pitch alone for left (blue) and right (green) eyes during detect and (K) track epochs. (L) Average (mean±SD) relationship between head roll and torsional eye rotations during detect epochs for left (blue) and right (green) eyes. Data from 57 epochs (4406 frames) from 3 animals. (M) Average head roll and torsional eye rotation relationship during track epochs. Conventions as in L. Data from 65 epochs (13624 frames) from 3 animals. (N) Performance of a model predicting torsion based on both head pitch and roll. Conventions as in J. For both J and N, data taken from 57 detect epochs (4406 frames), from 3 animals. (O) Performance of a model predicting torsion based on both head pitch and roll during tracking phases. For both K and O, data taken from 65 prey tracking epochs (13624 frames), from 3 animals.
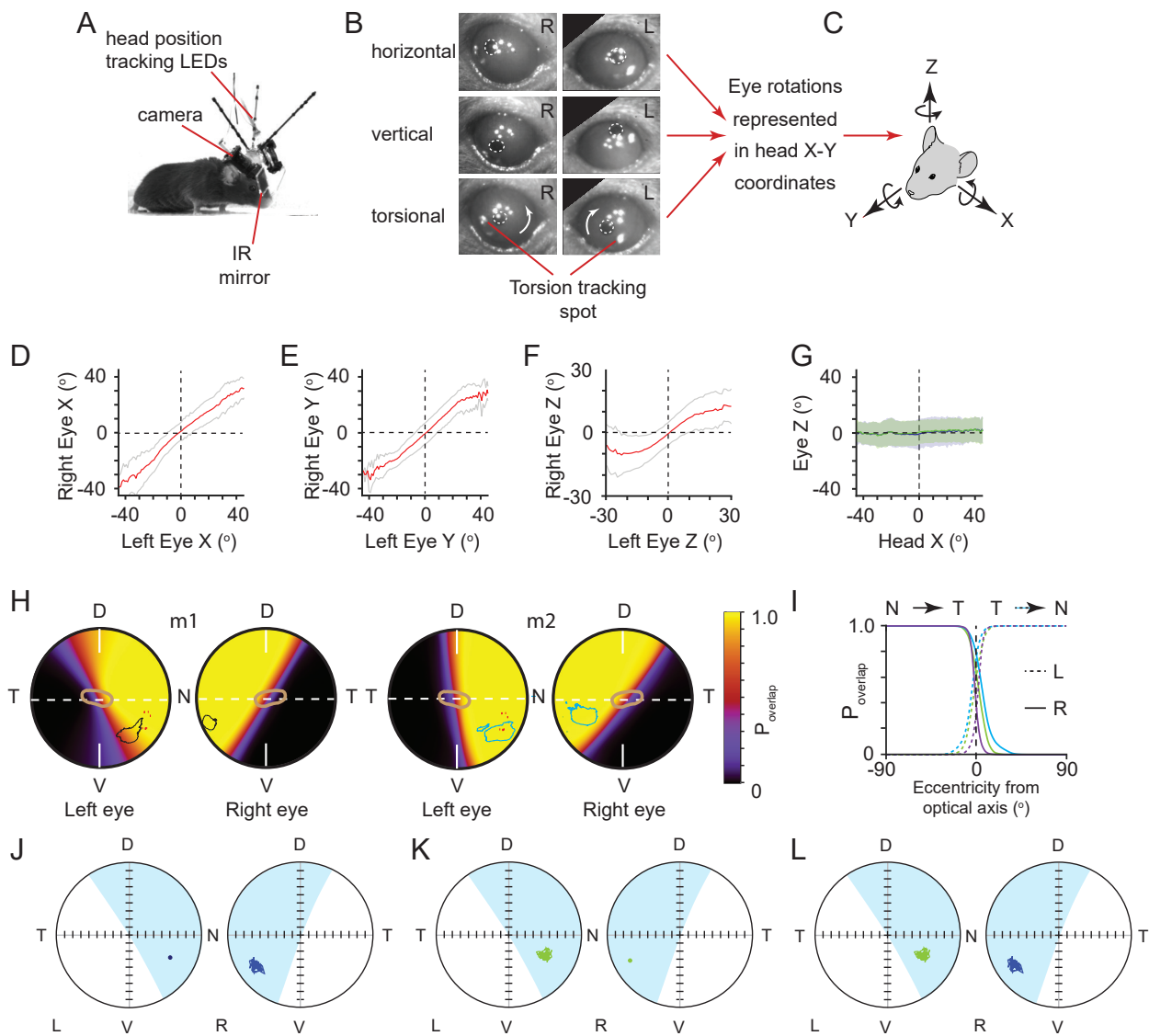
Figure 4 – figure supplement 3
VOR relationships between head and eye rotations and alignment of left and right eyes.
(A) Image of mouse with detachable miniaturized eye cameras and head position tracking system. **(B)** Example eye images showing horizontal, vertical and torsional eye rotations. Note TiO2 spots on the corneal surface for tracking torsion highlighted in lower panels. **(C)** Schematic of the common head and eye rotational axes. Relationship between **(D)** left and right eye X-rotations, **(E)** Y-rotations and **(F)** Z-rotations in common rotational axes. **(G)** Relationship between head X rotations and eye Z rotations for left eye (blue) and right eye (green). Data for D-G are represented as mean±SD, and are from 154500 frames from 3 animals. **(H)** Corneal view showing probability of overlap of left and right visual fields for two example animals m1 (left, 36449 frames) and m2 (right, 50874 frames), with overlay of isodensity contours (m1 -black, m2 - blue) from functional foci (see Figure 2 – figure supplement 1D) and contour of second highest RGC region (brown) from Figure 3B. **(I)** Profile of probability of overlap for left (dotted) and right (solid) eyes as a function of angular distance from optical axis for all three animals. Profile taken from horizontal axis through optical axis as shown in Figure 4D (dotted line in 4D, N = 3 animals, green = 36449 frames, blue = 50874 frames, purple = 71995 frames, respectively). **(J)** example of ocular alignment for the reference spot in the left eye projected into the right eye. **(K)** reference spot in the right eye projected into the left eye. **(L)** alignment over time for both reference spots.
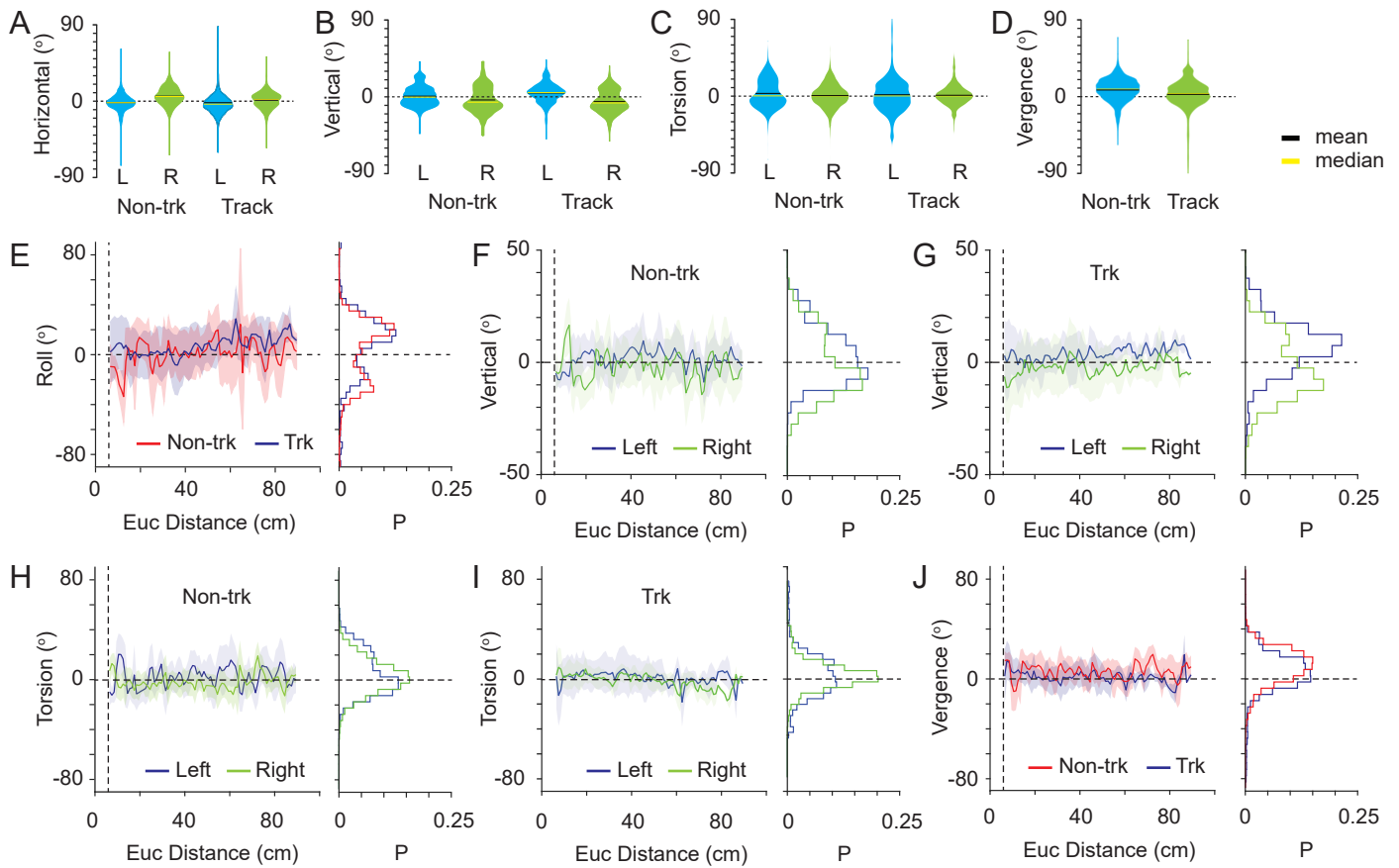
Figure 5 – figure supplement 1.
Eye movements during non-tracking and tracking periods.
(A) Violin plots showing the variability in horizontal eye rotations for left (blue) and right (green) eyes during non-tracking (Non-trk) and track (Track) epochs. **(B)** Variability in vertical eye rotations during non-tracking and track epochs. Conventions as in A. **(C)** Variability in torsional eye rotations during non-tracking and track epochs. Conventions as in A. **(D)** Variability in ocular vergence during non-tracking and track epochs. Conventions as in A. **(E)** Average relationship (mean±SD) between head roll and Euclidean distance from mouse to cricket during non-track (red) and track (blue) epochs. Data histogram shown at right. **(F)** Average relationship (mean±SD) between vertical eye rotations of left (blue) and right (green) eyes and Euclidean distance between mouse and cricket during non-track epochs. Data histogram shown at right. **(G)** Average relationship between vertical eye rotations and mouse-cricket Euclidean distance during track epochs. Conventions as in F. **(H)** Average relationship between torsional eye rotations and mouse-cricket Euclidean distance during non-track epochs. Conventions as in F. **(I)** Average relationship between torsional eye rotations and mouse-cricket Euclidean distance during non-track epochs. Conventions as in F. **(J)** Average relationship between ocular vergence and mouse-cricket Euclidean distance during non-tracking and tracking epochs. Conventions as in E. For all panels, data taken from 18 non-track epochs (15649 frames) and 18 track epochs (8510 frames), from 3 animals.